

HIERARCHICAL FORMATION OF GALAXIES WITH DYNAMICAL RESPONSE TO SUPERNOVA-INDUCED GAS REMOVAL

MASAHIRO NAGASHIMA¹

Division of Theoretical Astrophysics, National Astronomical Observatory, Mitaka, Tokyo 181-8588, Japan
Department of Physics, University of Durham, South Road, Durham DH1 3LE, U.K.

AND

YUZURU YOSHII

Institute of Astronomy, School of Science, The University of Tokyo, Mitaka, Tokyo 181-0015, Japan
Research Center for the Early Universe, School of Science, The University of Tokyo, Bunkyo-ku, Tokyo 113-0033, Japan

Draft version July 14, 2018

ABSTRACT

We reanalyze the formation and evolution of galaxies in the hierarchical clustering scenario. Using a semi-analytic model (SAM) of galaxy formation described in this paper, which we hereafter call the Mitaka model, we extensively investigate the observed scaling relations of galaxies among photometric, kinematic, structural and chemical characteristics. In such a scenario, spheroidal galaxies are assumed to be formed by major merger and subsequent starburst, in contrast to the traditional scenario of monolithic cloud collapse. As a new ingredient of SAMs, we introduce the effects of dynamical response to supernova-induced gas removal on size and velocity dispersion, which play an important role on dwarf galaxy formation. In previous theoretical studies of dwarf galaxies based on the monolithic cloud collapse given by Yoshii & Arimoto and Dekel & Silk, the dynamical response was treated in the extremes of a purely baryonic cloud and a baryonic cloud fully supported by surrounding dark matter. To improve this simple treatment, in our previous paper, we formulated the dynamical response in more realistic, intermediate situations between the above extremes. While the effects of dynamical response depend on the mass fraction of removed gas from a galaxy, how much amount of the gas remains just after major merger depends on the star formation history. A variety of star formation histories are generated through the Monte Carlo realization of merging histories of dark halos, and it is found that our SAM naturally makes a wide variety of dwarf galaxies and their dispersed characteristics as observed. It is also found that our result strongly depends on the adopted redshift dependence of star formation timescale, because it determines the gas fraction in high-redshift galaxies for which major mergers frequently occur. We test four star formation models. The first model has a constant timescale of star formation independent of redshift. The last model has a timescale proportional to the dynamical timescale of the galactic disk. The other models have timescales intermediates of these two. The last model fails to reproduce observations, because it predicts only little amount of the leftover gas at major mergers, therefore giving too weak dynamical response on size and velocity dispersion of dwarf spheroidals. The models, having a constant timescale of star formation or a timescale very weakly dependent on redshift, associated with our SAM, succeed to reproduce most observations from giant to dwarf galaxies, except that the adopted strong supernova feedback in this paper does not fully explain the color–magnitude relation under the cluster environment and the Tully–Fisher relation. A direction of overcoming this remaining problem is also discussed.

Subject headings: cosmology: theory – galaxies: dwarf – galaxies: evolution – galaxies: formation – large-scale structure of universe

1. INTRODUCTION

Dwarf galaxies give us many useful insights on the galaxy formation. They occupy a dominant fraction among galaxies in number and have a wide variety of structures and formation histories. Furthermore it would be easier to understand how physical processes such as heating by supernova explosions affect their evolution, because of shallowness of their gravitational potential well, compared to massive galaxies that have more complex formation histories and physical processes. Equally important is that massive galaxies have evolved via continuous mergers and accretion of less massive galaxies, according to the recent standard scenario of large-scale structure formation in the universe with the cold dark matter (CDM). This indicates that it is essential to understand

the formation of dwarf galaxies even in understanding the formation of massive galaxies, because they would be formed by mergers of their *building blocks* like dwarf galaxies.

Before the CDM model gained its popularity, traditional models of monolithic cloud collapse such as the galactic wind model for elliptical galaxies (Eggen, Lynden-bell & Sandage 1962; Larson 1969; Ikeuchi 1977; Saito 1979; Yoshii & Saio 1979; Arimoto & Yoshii 1986, 1987; Kodama & Arimoto 1997) and the infall model for spiral galaxies (Arimoto, Yoshii & Takahara 1991) had been widely used in analyses of galaxy evolution. These are simple but strong tools to explain various observations and then have contributed to construction of a basic picture of galaxy evolution. Based on such traditional models, Dekel & Silk (1986) systematically investigated many aspects of dwarf galaxies. Especially they focused on the role of supernova (SN) feedback, that is, heating up and sweeping out of the galactic gas by multiple SN explosions, in the

Electronic address: masa@scphys.kyoto-u.ac.jp

¹ Current address: Department of Physics, Graduate School of Science, Kyoto University, Sakyo-ku, Kyoto 606-8502, Japan

processes of formation and evolution of dwarf galaxies. Since a large amount of heated gas is expelled by the galactic wind, the self-gravitating system expands as a result of dynamical response to the gas removal (Hills 1980; Mathieu 1983; Vader 1986). They considered two limiting cases for the gas removal. One is a purely self-gravitating gas cloud, and another is a gas cloud embedded in a dominant dark halo. They showed that many observed scaling relations are well explained by their model. Combined with the evolutionary population synthesis code, Yoshii & Arimoto (1987) extended their analysis to estimating directly observable photometric properties, while only considering the purely self-gravitating gas cloud.

Since the hierarchical clustering of dark halos predicted by the CDM model becomes a standard structure formation scenario, the galaxy formation scenario must be modified so as to be consistent with the hierarchical merging of dark halos. Explicitly taking into account the Monte Carlo realization of merging histories of dark halos based on the distribution function of initial density fluctuations, the so-called semi-analytic models (SAMs) of galaxy formation have been developed (e.g., Kauffmann, White & Guiderdoni 1993; Cole et al. 1994; Baugh, Cole & Frenk 1996; Nagashima, Gouda & Sugiura 1999; Somerville & Primack 1999; Somerville, Primack & Faber 2001; Nagashima et al. 2001, 2002). SAMs include several important physical processes such as star formation, supernova feedback, galaxy merger, population synthesis and so on. While SAMs well reproduce many observed properties of galaxies, most of analyses have been limited to those of massive galaxies. Thus we focus on the formation of dwarf galaxies in the framework of the SAMs in this paper. In the analyses of dwarf galaxies, the dynamical response to gas removal, which is known to play an important role as shown by Dekel & Silk (1986) and Yoshii & Arimoto (1987), must be taken into account. While self-consistent equilibrium models taking into account baryon and dark matter have been analyzed by Yoshii & Saio (1987) and Ciotti & Pellegrini (1992), we focus on the dynamical response of baryons within a dark matter halo. Since we have derived the mathematical formula of dynamical response for the galaxies consisting of baryon and dark matter in Nagashima & Yoshii (2003), it is possible to incorporate them into our SAM.

The main purpose of this paper is a reanalysis of Dekel & Silk (1986) and Yoshii & Arimoto (1987) in the framework of SAMs. Thus we mainly focus on the formation of elliptical galaxies, which are assumed to be formed by major merger and subsequent starburst. In order to do this, we construct the Mitaka model, which is a SAM including the effects of dynamical response. So far many scaling relations among photometric, structural, and kinematical parameters of elliptical galaxies have been observed, such as the color-magnitude relation (e.g., Baum 1959), the velocity dispersion-magnitude relation (Faber & Jackson 1976), and the surface brightness-size relation (Kormendy 1977; Kodaira, Okamura & Watanabe 1983). To understand how these relations are originated, especially on scales of dwarf galaxies, helps to clarify the processes of galaxy formation and evolution in the context of the cosmological structure formation scenario. Although some authors found by principal component analysis that elliptical galaxies are distributed over the so-called fundamental plane in the three-dimensional space among photometric, structural and kinematical parameters (Watanabe, Kodaira & Okamura

1985; Dresler et al. 1987; Djorgovski & Davis 1987), we focus on the direct observables in this paper rather than their principal component projection.

This paper is outlined as follows. In §2 we describe our SAM. In §3 we constrain model parameters in our SAM using local observations. In §4 we compare the theoretical predictions of SAM galaxies with various observations. In §5 we examine consistency check of our SAM with other observations. In §6 we show the cosmic star formation history. In §7 we discuss the nature of galaxies on the cooling diagram that has been traditionally used for understanding the formation of galaxies. In §8 we provide summary and conclusion.

2. MODEL

The galaxy formation scenario that we use is as follows. In the CDM universe, dark matter halos cluster gravitationally and merge in a manner that depends on the adopted power spectrum of the initial density fluctuations. In each of the merged dark halos, radiative gas cooling, star formation, and gas reheating by supernovae occur. The cooled dense gas and stars constitute *galaxies*. These galaxies sometimes merge together in a common dark halo, and then more massive galaxies form. Repeating these processes, galaxies form and evolve to the present epoch.

Some ingredients of our SAM are revised. Modifications include the shape of mass function of dark halos, the star formation (SF) timescale, the merger timescale of galaxies taking into account the tidal stripping of subhalos, and the dynamical response to gas removal caused by starburst during major merger. The details are described below.

2.1. Merging Histories of Dark Halos

The merging histories of dark halos are realized by a Monte Carlo method proposed by Somerville & Kolatt (1999), based on the extended Press-Schechter (PS) formalism (Bond et al. 1991; Bower 1991; Lacey & Cole 1993). This formalism is an extension of the Press-Schechter formalism (Press & Schechter 1974), which gives the mass function of dark halos, $n(M)$, to estimate the mass function of progenitor halos with mass M_1 at a redshift $z_0 + \Delta z$ of a single dark halo with mass M_0 collapsing at a redshift z_0 , $n(M_1; z_0 + \Delta z | M_0; z_0) dM_1$. According to this mass function, a set of progenitors is realized. By repeating this, we obtain a *merger tree*. Realized trees are summed with a weight given by a mass function at output redshift. Dark halos with circular velocity $V_{\text{circ}} \geq V_{\text{low}} = 30 \text{ km s}^{-1}$ are regarded as isolated halos, otherwise as diffuse accreted matter.

In our previous papers, we adopted the PS mass function to provide the weight for summing merger trees. Recent high-resolution N -body simulations, however, suggest that the PS mass function should be slightly corrected (e.g., Jenkins et al. 2001). According to the notation in Jenkins et al. (2001), the original PS mass function is written by

$$f(\sigma; \text{PS}) = \sqrt{\frac{2}{\pi}} \frac{\delta_c}{\sigma} \exp\left(-\frac{\delta_c^2}{2\sigma^2}\right), \quad (1)$$

and the cumulative mass function $n(M)$ is related with the above function by

$$f(\sigma; X) = \frac{M}{\rho_0} \frac{dn(M)}{d \ln \sigma^{-1}}, \quad (2)$$

where X specifies a model such as PS, ρ_0 is the mean density of the universe, σ denotes the standard deviation of the

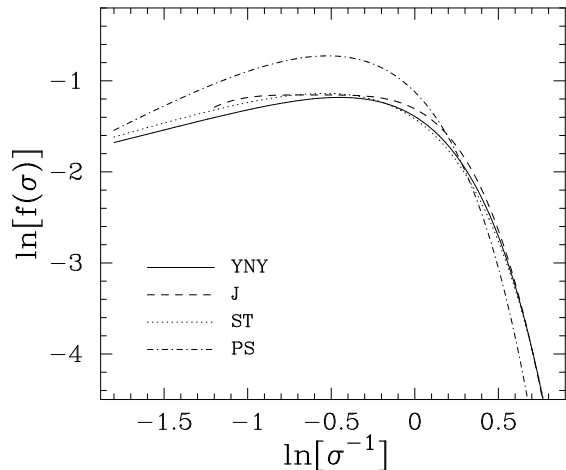


FIG. 1.— Mass functions of dark halos. The solid line represents the mass function given by Yahagi, Nagashima & Yoshii (2003, YNY), which is used in this paper. The dot-dashed line is the original PS mass functions, respectively. The dotted line is the analytic result by Sheth & Tormen (1999, ST). The dashed line is the N -body result over the resolved range by Jenkins et al. (2001, J).

density fluctuation field, and δ_c is the critical density contrast for collapse assuming spherically symmetric collapse (Tomita 1969; Gunn & Gott 1972). In this paper we use the following mass function given by Yahagi, Nagashima & Yoshii (2003, hereafter YNY) instead of the PS mass function,

$$f(\sigma; \text{YNY}) = A(1 + x^C)x^D \exp(-x^2), \quad (3)$$

where $x = B\delta_c/\sqrt{2}\sigma$, $A = 2/[\Gamma(D/2) + \Gamma(\{C + D\}/2)]$, $B = 0.893$, $C = 1.39$ and $D = 0.408$. This is a fitting function that satisfies the normalization condition, that is, the integration over all range of ν is unity. These functions are plotted in Figure 1 by the solid line (YNY) and the dot-dashed line (PS). We also show other often used formula given by Sheth & Tormen (1999),

$$f(\sigma; \text{ST}) = A\sqrt{\frac{2a}{\pi}} \left[1 + \left(\frac{\sigma^2}{a\delta_c^2} \right)^p \right] \frac{\delta_c}{\sigma} \exp\left(-\frac{a\delta_c^2}{2\sigma^2}\right), \quad (4)$$

and by Jenkins et al. (2001),

$$f(\sigma; \text{J}) = 0.315 \exp(-|\ln \sigma^{-1} + 0.61|^{3.8}), \quad (5)$$

where $A = 0.3222$, $a = 0.707$ and $p = 0.3$ for the former (ST) and the latter (J) formula is valid over the range $-1.2 \leq \ln \sigma^{-1} \leq 1.05$.

The number density of dark halos with large mass given by the above three functions (YNY, ST and J) and by the N -body simulation are similar to those given by analytic estimation (e.g., Yano, Nagashima & Gouda 1996; Monaco 1998; Nagashima 2001) and are therefore trustworthy. With N -body simulations, it is difficult to estimate the mass function at low mass because of the limited resolution and the uncertainty in the identification of dark halos. The very high resolution N -body simulations, made using the adaptive mesh refinement method by Yahagi & Yoshii (2001) and Yahagi (2002), predict a mass function similar to that of ST. This mass function extends to a mass 10 times smaller than that of Jenkins et al. (2001) and has a slightly different slope. Thus we adopt the YNY mass function as above. A comparison between the YNY mass function and the N -body simulation is discussed in a separate paper (Yahagi, Nagashima & Yoshii 2003). In

§3 we show how the mass function of dark halos affects the luminosity function of galaxies.

In short, we realize merger trees by using the extended PS formalism for dark halos whose mass function is given by the YNY at each output redshift.

In this paper, we only consider a recent standard Λ CDM model, that is, $\Omega_0 = 0.3$, $\Omega_\Lambda = 0.7$, $h = 0.7$ and $\sigma_8 = 0.9$, where these parameters denote the mean density of the universe, the cosmological constant, the Hubble parameter and the normalization of the power spectrum of the initial density fluctuation field. The shape of the power spectrum given by Sugiyama (1995), which is a modified one of Bardeen et al. (1986, hereafter BBKS) taking into account the baryonic effects, is adopted.

2.2. Tidal Stripping of Subhalos

Most of recent high resolution N -body simulations suggest that swallowed dark halos survive in their host halo as *subhalos*. Envelopes of those subhalos are stripped by tidal force from the host halo. We assume the radius of a tidally stripped subhalo r_t by

$$\frac{r_t}{r_s} = \frac{r_{\text{peri}}}{r_{\text{apo}}} \frac{M_h}{M_s} \left(\frac{V_{\text{circ},s}}{V_{\text{circ},h}} \right)^3, \quad (6)$$

where r_{peri} and r_{apo} are the pericenter and apocenter for the orbit of the subhalo, respectively, and subscripts “h” and “s” indicate the host halo and subhalo, respectively. In this paper, a ratio of $r_{\text{peri}}/r_{\text{apo}} = 0.2$ is assumed (Ghigna et al. 1998; Okamoto & Habe 1999, 2000). Because a singular isothermal profile for subhalos is assumed, their mass decreases proportional to r_t/r_s . The mass of stripped subhalos is used in the estimation of dynamical response to gas removal on the size and velocity dispersion when satellite galaxies merge together (see §§2.5).

2.3. Gas Cooling, Star Formation and Supernova Feedback

The mean mass density in dark halos is assumed to be proportional to the cosmic mean density at the epoch of collapse using a spherically symmetric collapse model (Tomita 1969; Gunn & Gott 1972). Each collapsing dark halo contains baryonic matter with a mass fraction Ω_b/Ω_0 , where Ω_b is the baryon density parameter. We adopt a value of $\Omega_b h^2 = 0.02$ that is recently suggested by the BOOMERANG Project measuring the anisotropy of the cosmic microwave background (Netterfield et al. 2002). This value is an intermediate one between $(0.64 - 1.4) \times 10^{-2}$ given by analysis of light element abundance produced by big bang nucleosynthesis (Suzuki, Yoshii & Beers 2000) and $(2.24 \pm 0.09) \times 10^{-2}$ given by analysis of cosmic microwave background observed by *WMAP* (Spergel et al. 2003). The baryonic matter consists of diffuse hot gas, dense cold gas, and stars.

When a halo collapses, the hot gas is shock-heated to the virial temperature of the halo with an isothermal density profile. A part of the hot gas cools and accretes to the disk of a galaxy until subsequent collapse of dark halos containing this halo. The amount of the cold gas involved is calculated by using metallicity-dependent cooling functions provided by Sutherland & Dopita (1993). The difference of cooling rates between the primordial and metal-polluted gases is prominent at $T \sim 10^6 \text{K}$ due to line-cooling of metals. Chemical enrichment in hot gas is consistently solved with star formation and SN feedback. The cooling is, however, very efficient in dark halos with a virial temperature of $T \sim 10^6 \text{K}$ even in the case

of the primordial gas, so the metallicity dependence of cooling rate only slightly affects our results. In order to avoid the formation of unphysically large galaxies, the cooling process is applied only to halos with $V_{\text{circ}} \leq V_{\text{cut}} = 250 \text{ km s}^{-1}$. This manipulation would be needed, because the simple isothermal distribution forms so-called ‘‘monster galaxies’’ due to too efficient cooling at the center of halos. While Cole et al. (2000) adopted another isothermal distribution with central core instead of such a simple cutoff of the cooling and Benson et al. (2003b) considered some additional mechanisms such as the heating of hot gas by SNe and by heat conduction from outside as well as its removal by superwinds from halos, we take the above simple approach. The value of V_{cut} is rather small compared with our previous paper and other SAMs. This is caused by our assumption that invisible stars have negligible fraction, which is introduced to darken luminosity of galaxies (§§2.6). This smaller value of V_{cut} makes the color of large galaxies less red, which shows up on a bright portion of the color-magnitude relation of elliptical galaxies (§§5.5).

Stars in disks are formed from the cold gas. The SF rate (SFR) \dot{M}_* is given by the cold gas mass M_{cold} and a SF timescale τ_* as $\dot{M}_* = M_{\text{cold}}/\tau_*$. Now we consider two SF models. One is a constant star formation (CSF), in which τ_* is constant against redshift. Another is a dynamical star formation (DSF), in which τ_* is proportional to the dynamical timescale of the halo, which allows for the possibility that the SF efficiency is variable with redshift. We then express these SF timescales as

$$\tau_* = \begin{cases} \tau_*^0 [1 + \beta(V_{\text{circ}})] & (\text{CSF}), \\ \tau_*^0 [1 + \beta(V_{\text{circ}})] \left[\frac{\tau_{\text{dyn}}(z)}{\tau_{\text{dyn}}(0)} \right] (1+z)^\sigma & (\text{DSF}), \end{cases} \quad (7)$$

where τ_*^0 and σ are free parameters, and β indicates the ratio of the SF timescale to the reheating timescale by the SN feedback defined by equation (9) (see below). Pure DSF occurs when $\sigma = 0$. Because the timescale of cold gas consumption is equal to $\tau_*/(1+\beta-R)$, where R is the returned mass fraction from evolved stars ($R = 0.25$ in this paper), the mass fraction of cold gas in galaxies that is nearly constant against their magnitude is automatically adjusted by multiplying $(1+\beta)$. Hence the parameter α_* originally introduced by Cole et al. (1994) is eliminated by introducing the factor $(1+\beta)$. The parameter τ_*^0 is so chosen as to match the mass fraction of cold gas with the observed fraction (see §3). Thereby the SF-related parameters are constrained according to Cole et al. (2000). Since not all of cold gas might be observed, the observed data give a lower limit to mass fraction of cold gas.

Figure 2 shows the redshift dependence of SF timescale for the four SF models of CSF (dot-dashed line), DSF0 ($\sigma = 0$; solid line), DSF1 ($\sigma = 0.5$; dotted line) and DSF2 ($\sigma = 1$; dashed line). Objects, which collapse at higher redshift, have higher density and therefore shorter dynamical timescale. Evidently, the DSF with smaller σ gives more rapid conversion of cold gas into stars, compared with the CSF. The four SF models predict different mass fraction of cold gas at high redshift, leading to quite different characteristics of dwarf galaxies. This indicates, as will be clarified later, that the redshift dependence of SF timescale can be constrained particularly from observed structures and photometric properties of dwarf galaxies.

Massive stars explode as Type II SNe and heat up the surrounding cold gas. This SN feedback reheats the cold gas at a rate of $\dot{M}_{\text{reheat}} = M_{\text{cold}}/\tau_{\text{reheat}}$, where the timescale of reheating

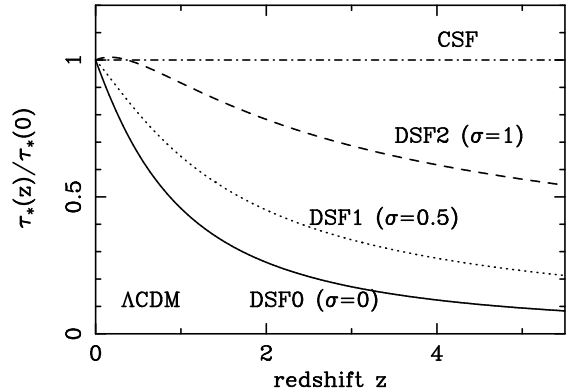


FIG. 2.— Star formation timescales τ_* as a function of redshift z in a Λ CDM model. The timescale is normalized to unity at the present epoch. The dot-dashed line represent the constant SF model (CSF). The solid, dotted and dashed lines represent the variants of dynamical SF model with $\sigma = 0$ (DSF0), 0.5 (DSF1) and 1 (DSF2), respectively, according to the prescriptions in equation 7.

is given by

$$\tau_{\text{reheat}} = \frac{\tau_*}{\beta(V_{\text{circ}})}, \quad (8)$$

where

$$\beta(V_{\text{circ}}) \equiv \left(\frac{V_{\text{circ}}}{V_{\text{hot}}} \right)^{\alpha_{\text{hot}}}. \quad (9)$$

The free parameters V_{hot} and α_{hot} are determined by matching the local luminosity function of galaxies with observations.

With the above equations and parameters, we obtain the masses of hot gas, cold gas, and disk stars as a function of time or redshift. Chemical enrichment is also taken into account, adopting the *heavy-element yield* of $y = 2Z_{\odot}$, assuming the instantaneous recycling approximation with the returned mass fraction from evolved stars $R = 0.25$. All of newly produced metals are released into cold gas, then by SN feedback, a part of them is expelled into hot gas. Some metals in hot gas are brought back to cold gas by subsequent cooling, and are accumulated in stars by their formation.

2.4. Mergers of dark halos and galaxies

When two or more progenitor halos have merged, the newly formed larger halo should contain at least two or more galaxies which had originally resided in the individual progenitor halos. By definition, we identify the central galaxy in the new common halo with the central galaxy contained in the most massive one of the progenitor halos. Other galaxies are regarded as satellite galaxies. These satellites merge by either dynamical friction or random collision. The timescale of merging by dynamical friction is given by $\tau_{\text{mrg}} = f_{\text{mrg}} \tau_{\text{fric}}$, where τ_{fric} is given by Binney & Tremaine (1987), which is estimated from masses of the new common halo and the tidally truncated subhalo. The parameter f_{mrg} is set to 0.7 in this paper. When the time elapsed after merging of a progenitor halo exceeds τ_{mrg} , the satellite galaxy is accreted to the central galaxy. On the other hand, the mean free timescale of random collision of satellite galaxies τ_{coll} is given by Makino & Hut (1997). With a probability $\Delta t/\tau_{\text{coll}}$, where Δt is the time step corresponding to the redshift interval Δz of merger tree of dark halos, a satellite galaxy merges with another satellite picked out randomly (Somerville & Primack 1999).

Consider the case when two galaxies of masses m_1 and $m_2 (> m_1)$ merge together. If the mass ratio $f = m_1/m_2$ is larger than a certain critical value of f_{bulge} , we assume that a starburst occurs and that all of the cold gas turns into stars and hot gas, which fills the resulting halo, and all of the stars populate the bulge of a new galaxy. On the other hand, if $f < f_{\text{bulge}}$, no starburst occurs, and a smaller galaxy is simply absorbed into the disk of a larger galaxy. Throughout this paper we use $f_{\text{bulge}} = 0.5$, which gives a consistent morphological fraction in galaxy number counts.

2.5. Size of Galaxies and Dynamical Response to Starburst-induced Gas Removal

We assume that the size of spiral galaxies is determined by a radius at which the gas is supported by rotation, under the conservation of specific angular momentum of hot gas that cools and contracts. We also assume that the initial specific angular momentum of the gas is the same as that of the host dark halo. Acquisition of the angular momentum of dark halos is determined by tidal torques in the initial density fluctuation field (White 1984; Catelan & Theuns 1996a,b; Nagashima & Gouda 1998). The distribution of the dimensionless spin parameter λ_H , which is defined by $\lambda_H \equiv L|E|^{1/2}/GM^{5/2}$ where L is the angular momentum and E is the binding energy, is well approximated by a log-normal distribution (Mo, Mao & White 1998),

$$p(\lambda_H)d\lambda_H = \frac{1}{\sqrt{2\pi}\sigma_\lambda} \exp\left[-\frac{(\ln\lambda_H - \ln\bar{\lambda})^2}{2\sigma_\lambda^2}\right] d\ln\lambda_H, \quad (10)$$

where $\bar{\lambda}$ is the mean value of spin parameter and σ_λ is its logarithmic variance. We adopt $\bar{\lambda} = 0.03$ and $\sigma_\lambda = 0.5$. When the specific angular momentum is conserved, the effective radius r_e of a presently observed galaxy at $z=0$ is related to the initial radius R_i of the progenitor gas sphere via $r_e = (1.68/\sqrt{2})\lambda_H R_i$ (Fall 1979; Fall & Efstathiou 1980; Fall 1983). The initial radius R_i is set to be the smaller one between the virial radius of the host halo and the cooling radius. A disk of a galaxy grows due to cooling and accretion of hot gas from more distant envelope of its host halo. In our model, when the estimated radius by the above equation becomes larger than that in the previous time-step, the radius grows to the new larger value in the next step. At that time, the disk rotation velocity V_d is set to be the circular velocity of its host dark halo.

Size estimation of high-redshift spiral galaxies, however, carries uncertainties because of the large dispersion in their observed size distribution. For example, Simard et al. (1999) suggests only mild evolution of disk size against redshift, taking into account the selection effects arising from the detection threshold of surface brightness, although the above simple model predicts disk size proportional to virial radius R_{vir} of host dark halos evolving as $R_{\text{vir}} \propto 1/(1+z)$ for fixed mass. Allowing for the possibility that the conservation of angular momentum is not complete, we generalize this size estimation by introducing a simple redshift dependence,

$$r_e = \frac{1.68}{\sqrt{2}} \lambda_H R_i (1+z)^\rho, \quad (11)$$

where ρ is a free parameter. We simply use $\rho = 1$ as a reference value in this paper. The effect of changing ρ emerges in the selection effects due to the cosmological dimming of surface brightness and in the dust extinction, because the dust column density also changes with galaxy size. This is discussed in §5.

Size of early-type galaxies, which likely form from galaxy mergers, are primarily determined by the virial radius of the baryonic component. When a major merger of galaxies occurs, assuming the energy conservation, we estimate the velocity dispersion of the merged system. Now we assign the subscript 0 to the merged galaxy, and subscripts 1 and 2 to the central and satellite galaxies, respectively, in the case of central-satellite merger, or to larger and smaller galaxies, respectively, in the case of satellite-satellite merger. Using the virial theorem, the total energy for each galaxy is

$$E_i = -\frac{1}{2}[M_b V_b^2 + (M_d + M_{\text{cold}})V_d^2], \quad (12)$$

where M_b and M_d are the masses of bulge and disk, respectively, and V_b and V_d are the velocity dispersion of bulge and the rotation velocity of disk, respectively. Assuming the virial equilibrium, the binding energy E_b between the progenitors just before the merger is given by

$$E_b = -\frac{E_1 E_2}{(M_2/M_1)E_1 + (M_1/M_2)E_2}. \quad (13)$$

Then we obtain

$$E_1 + E_2 + E_b = E_0. \quad (14)$$

Just after the merger there is only the bulge component consisting of cold gas and stars in the merger remnant, whose velocity dispersion is directly estimated from the above equation. This procedure is similar to Cole et al. (2000), although they argued it in terms of size estimation. Then the size of the system just after the merger is defined by

$$r_i = \frac{GM_i}{2V_b^2}, \quad (15)$$

where $M_i = M_* + M_{\text{cold}}$ is the total baryonic mass of the merged system.

Next, the cold gas turns into stars and hot gas. Newly formed stellar mass is nearly equal to $M_{\text{cold}}/(1+\beta)$ and the rest of the cold gas is expelled from the merged system to the halo by SN feedback. The final mass after the mass loss, M_f , can be estimated from the known β . Assuming the density distributions of baryonic and dark matters, the dynamical response on the structural parameters to the mass loss can be estimated. In this paper we adopt the Jaffe model (Jaffe 1983) for baryonic matter and the singular isothermal sphere for dark matter, and assume slow (adiabatic) gas removal compared with dynamical timescale of the system. Defining the ratios of mass, size, density and velocity dispersion at final state relative to those at initial state by \mathcal{M}, R, Y and U , the response under the above assumption is approximately given by

$$R \equiv \frac{r_f}{r_i} = \frac{1+D/2}{\mathcal{M}+D/2}, \quad (16)$$

$$U \equiv \frac{V_{b,f}}{V_{b,i}} = \sqrt{\frac{YR^2 + Df(z_f)/2}{1 + Df(z_i)/2}}, \quad (17)$$

where $\mathcal{M} = YR^3$, $D = 1/y_i z_i^2$, y and z are the ratios of density and size of baryonic matter to those of dark matter and, $f(z)$ is a function defined in Appendix. The subscripts i and f stand for the initial and final states in the mass loss process. The details are shown in Appendix and Nagashima & Yoshii (2003). The parameter D indicates the contribution of dark matter to the gravitational potential felt by baryonic matter in

the central region of a halo. In actual calculation, we use a circular velocity at the center of dark halos, V_{cent} defined below, to estimate D as $2V_{\text{cent}}^2/V_{b,i}^2$, instead of the ratios of size y_i and density z_i which characterize the global property of dark halos. If there is negligible dark matter ($D \rightarrow 0$), the well-known result of adiabatic invariant $(M_* + M_{\text{cold}})r$ emerges (e.g., Yoshii & Arimoto 1987). In contrast, if there is negligible baryonic matter ($D \rightarrow \infty$), R and U become unity, that is, size and velocity dispersion do not change during mass loss. The effect of the dynamical response is the most prominent for dwarf galaxies of low circular velocity.

Considering realistic situations, the baryonic matter often condenses in the central region and becomes denser than the average density in the halo. It is likely that the depth of gravitational potential well is changed when a part of baryonic mass is removed due to SN feedback. To take into account this process, we define a central circular velocity of dark halo V_{cent} . When a dark halo collapses without any progenitors, V_{cent} is set to V_{circ} . After that, although the mass of the dark halo grows up by subsequent accretion and/or mergers, V_{cent} remains constant or decreases by the dynamical response. When the mass is doubled, V_{cent} is set to V_{circ} at that time again. The dynamical response to mass loss from a central galaxy of a dark halo by SN feedback lowers V_{cent} of the dark halo as follows:

$$\frac{V_{\text{cent},f}}{V_{\text{cent},i}} = \frac{M_f/2 + M_d(r_i/r_d)}{M_i/2 + M_d(r_i/r_d)}. \quad (18)$$

The change of V_{cent} in each time step is only a few per cent. Under these conditions the approximation of static gravitational potential of dark matter is valid during starburst.

Once a dark halo falls into its host dark halo, it is treated as a subhalo. Because we assume that subhalos do not grow up in mass, the central circular velocity of the subhalos monotonically decreases. Thus this affects the dynamical response later when mergers between satellite galaxies occur. We approximate that the resultant density distribution remains to be isothermal with V_{cent} at least within the galaxy size.

2.6. Photometric Properties and Morphological Identification

The above processes are repeated until the output redshift and then the SF history of each galaxy is obtained. For the purpose of comparison with observations, we use a stellar population synthesis approach, from which the luminosities and colors of model galaxies are calculated. Given the SFR as a function of time or redshift, the absolute luminosity and colors of individual galaxies are calculated using a population synthesis code by Kodama & Arimoto (1997). The stellar metallicity grids in the code cover a range from $Z_* = 0.0001$ to 0.05. Note that we now define the metallicity as the mass fraction of metals. The initial stellar mass function (IMF) that we adopt is the power-law IMF of Salpeter form, with lower and upper mass limits of $0.1M_{\odot}$ and $60M_{\odot}$, respectively.

In most of SAM analyses, it has been assumed that there is a substantial fraction of invisible stars such as brown dwarfs. Cole et al. (1994) introduced a parameter defined as $\Upsilon = (M_{\text{lum}} + M_{\text{BD}})/M_{\text{lum}}$, where M_{lum} is the total mass of luminous stars with mass larger than $0.1M_{\odot}$ and M_{BD} is that of invisible brown dwarfs. A range of $\Upsilon \sim 1 - 3$ has been assumed depending on ingredients of SAMs. For example, Cole et al. (2000) assumed $\Upsilon = 3.07$ in the case of $\Omega_b = 0.04$. In this paper, however, we do not assume the existence of substantial fraction of invisible stars. If a large value of Υ is adopted, the

mass-to-light ratio of galaxies is too high to agree with observations. Thus we fix $\Upsilon = 1$. Somerville & Primack (1999) also adopted a small value of $\Upsilon = 1.25$ in their Λ CDM.3 model for $\Omega_b = 0.037$ (in their notation $f_{\text{lum}}^* = 1/\Upsilon = 0.8$).

The optical depth of internal dust is consistently estimated by our SAM. We take the usual assumption that the abundance of dust is proportional to the metallicity of cold gas, and then the optical depth is proportional to the column density of metals. Then the optical depth τ is given by

$$\tau \propto \frac{M_{\text{cold}}Z_{\text{cold}}}{r_e^2}, \quad (19)$$

where r_e is the effective radius of the galactic disk. There are large uncertainties in estimating the proportionality constant, but we adopt about a factor of two smaller value compared with that in Cole et al. (2000), otherwise it predicts too strong extinction to reproduce galaxy number counts, presumably because our chemical yield is higher than theirs. Wavelength dependence of optical depth is assumed to be the same as the Galactic extinction curve given by Seaton (1979). Dust distribution is simply assumed to be the slab dust (Disney, Davies & Phillipps 1989), according to our previous papers. We found that the resultant mean extinction for spiral galaxies is close to a model by Cole et al. (2000).

We classify galaxies into different morphological types according to the B -band bulge-to-disk luminosity ratio B/D . In this paper, following Simien & de Vaucouleurs (1986), galaxies with $B/D \geq 1.52$, $0.68 \leq B/D < 1.52$, and $B/D < 0.68$ are classified as elliptical, lenticular, and spiral galaxies, respectively. Kauffmann, White & Guiderdoni (1993) and Baugh, Cole & Frenk (1996) showed that this method of type classification well reproduces the observed type mix.

3. PARAMETER SETTINGS

As already mentioned, we adopt a standard Λ CDM model. The cosmological parameters are $\Omega_0 = 0.3$, $\Omega_{\Lambda} = 0.7$, $h = 0.7$ and $\sigma_8 = 0.9$. The baryon density parameter $\Omega_b = 0.02h^{-2}$ is used.

The astrophysical parameters are constrained from local observations, according to the procedure discussed in Nagashima et al. (2001, 2002). The adopted values are slightly different from those in our previous papers. This is mainly caused by adopting the different mass function of dark halos (§2.1) and by fixing $\Upsilon = 1$ (§2.6). Values of these parameters are tabulated in Tables 1 and 2.

First, the SN feedback-related parameters (V_{hot} , α_{hot}) and merger-related parameter (f_{mrg}) are almost uniquely determined if their values are so chosen as to reproduce the local luminosity function. Figure 3 shows theoretical results for CSF (solid line), DSF2 (dashed line), DSF1 (dot-dashed line) and DSF0 (dotted line). As in our previous papers, the SF timescale affects the local luminosity function only slightly. Symbols with errorbars represent observational results from the B -band redshift surveys, such as Automatic Plate Machine (APM; Loveday et al. 1992), ESO Slice Project (ESP; Zucca et al. 1997), Durham/United Kingdom Schmidt Telescope (UKST; Ratcliffe et al. 1998) and Two-Degree Field (2dF; Folkes et al. 1999), and from the K -band redshift surveys given by Szokoly et al. (1998), Two Micron All Sky Survey (2MASS; Kochanek et al. 2001) and 2dF combined with 2MASS (Cole et al. 2001).

In Figure 3 we see how the mass function of dark halos affects the luminosity function. In the same figure we show the same model as CSF but for the PS mass function represented by the thin solid lines. As the PS mass function

TABLE 1
 STANDARD SETTINGS OF ASTROPHYSICAL PARAMETERS IN THE MITAKA MODEL

Parameter	Value	Annotation	Observation
V_{hot}	150 km s^{-1}	supernova feedback-related (§§2.3)	luminosity functions (Figure 3)
α_{hot}	4		
V_{cut}	250 km s^{-1}	cooling cut-off (§§2.3)	luminosity functions (Figure 3)
V_{low}	30 km s^{-1}	minimum circular velocity of dark halos (§§2.1)	—
y	$2 Z_{\odot}$	heavy-element yield (§§2.3)	metallicity distribution (Figure 18)
f_{bulge}	0.5	major/minor merger criterion (§§2.4)	morphological counts
f_{img}	0.7	coefficient of dynamical friction timescale (§§2.4)	luminosity functions (Figure 3)
$\bar{\lambda}$	0.03	spin parameter distribution (§§2.5)	disk size (Figure 5)
σ_{λ}	0.5		
ρ	1	redshift dependence of disk size (§§2.5)	faint galaxy number counts (Figures 20 and 21)
Υ	1	fraction of invisible stellar mass (§§2.6)	mass-to-light ratio (Figure 17)

NOTE. — Cosmological parameters are: $(\Omega_0, \Omega_{\Lambda}, h, \sigma_8, \Omega_b) = (0.3, 0.7, 0.7, 0.9, 0.02 h^{-2})$.

 TABLE 2
 STAR
 FORMATION-MODEL
 DEPENDENT
 PARAMETERS

Model	τ_*^0 (Gyr)	σ
CSF	1.3	—
DSF0	1.7	0
DSF1	1.3	0.5
DSF2	1.5	1

NOTE. — τ_*^0 is determined by matching the mass fraction of cold gas with the observed fraction in spiral galaxies [equation 7 and Figure 4].

predicts more dark halos and hence more galaxies than the YNY mass function except for the largest mass scale. Thus, we need $V_{\text{hot}} = 150 \text{ km s}^{-1}$, less than 280 km s^{-1} in the previous model, to weaken SN feedback which mainly determines the scale of the exponential cut-off of the luminosity function (Nagashima et al. 2001, 2002). We also investigated the effects of power spectrum of density fluctuations and confirmed that neither a $\sigma_8 = 1$ model nor a model with BBKS power spectrum without the baryonic effects is significantly different from our reference model. In §5, we discuss the slight effect that σ_8 has on high-redshift galaxies.

The effects of photoionization on the luminosity function have been discussed (Chiba & Nath 1994; Nagashima, Gouda & Sugiura 1999; Bullock, Kravtsov & Weinberg 2000; Nagashima & Gouda 2001; Somerville 2002; Tully et al. 2002; Benson et al. 2002a,b, 2003a). There are two ways to suppress the gas cooling by photoionization. One effect is that the ultraviolet (UV) background from quasars and/or young stars prevents hot gas at the outer envelope from cooling. Another is that the Jeans mass becomes larger after cosmic reionization, which means larger V_{low} . It has been found that both processes lower the faint-end of the luminosity function. For example, if we use a large value of $V_{\text{low}} \simeq 70 \text{ km s}^{-1}$ for our model, which corresponds to increasing the Jeans mass, the number of galaxies at the faint-end of the resultant luminosity function decreases by about a factor of two, less than that

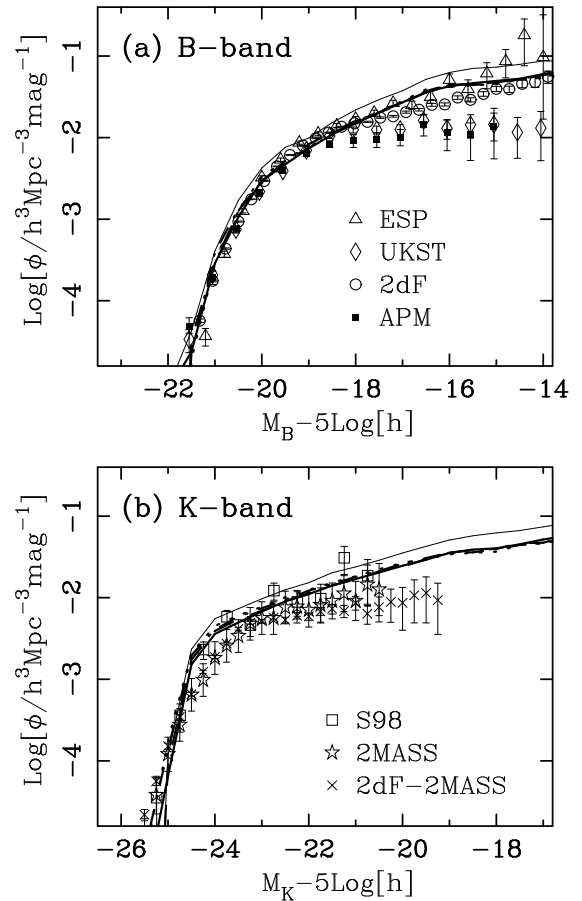


FIG. 3.— Local luminosity functions in the (a) B band and (b) K band. The thick solid, dashed, dot-dashed, and dotted lines represent the models of CSF, DSF2, DSF1, and DSF0, respectively, based on the YNY mass function. Only for the purpose of comparison here, shown by the thin solid line is the CSF model based on the original PS mass function. Symbols with error bars in (a) indicate the observational data from APM (Loveday et al. 1992, filled squares), ESP (Zucca et al. 1997, open triangles), Durham/UKST (Ratcliffe et al. 1998, open diamonds), and 2dF (Folkes et al. 1999, open circles). Symbols in (b) indicate the data from Szokoly et al. (1998, open squares), 2MASS (Kochanek et al. 2000, open stars), and 2dF combined with 2MASS (Cole et al. 2000, crosses).

given by the APM survey at $-20 \lesssim M_B - 5 \log(h) \lesssim -17$ (see Figure 3). In that case we need weaker SN feedback,

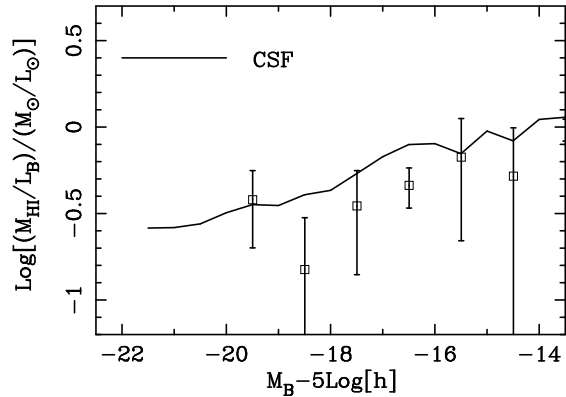


FIG. 4.— Cold gas mass relative to B -band luminosity of spiral galaxies. The solid line represents the CSF model. Other SF models, not shown, give almost the same results with only 0.1 dex difference. The open squares indicate the observational data for atomic neutral hydrogen taken from Huchtmeier & Richter (1988). Since the cold gas in the model consists of all species of elements, its mass is multiplied by 0.75, i.e., $M_{\text{HI}} = 0.75M_{\text{cold}}$, which corresponds to a total fraction of atomic and molecular hydrogen. Therefore, in comparison with the theoretical result, the observational data should be regarded as lower limits.

that is, smaller V_{hot} and/or smaller α_{hot} . We found, however, that such a large value of V_{low} does not make dwarf spheroidals at $M_B - 5 \log(h) \gtrsim -12$ for $V_{\text{low}} = 70 \text{ km s}^{-1}$ and at $M_B - 5 \log(h) \gtrsim -10$ for $V_{\text{low}} = 50 \text{ km s}^{-1}$. In addition, giant galaxies obtain more gas that has not cooled in smaller halos $V_{\text{circ}} \leq V_{\text{low}}$, causing the bright-end of the luminosity function to shift brighter. Note that this is not effective for $V_{\text{low}} \lesssim 40 \text{ km s}^{-1}$. Keeping in mind that such effects might affect our analysis through the determination of SN feedback-related parameters, we use $V_{\text{low}} = 30 \text{ km s}^{-1}$ in this paper.

Next, the SFR-related parameter (τ_*^0) is determined by using the mass fraction of cold gas in spiral galaxies. The gas fraction depends on both the SN feedback-related and SFR-related parameters. The former parameters determine the gas fraction expelled from galaxies and the latter the gas fraction that is converted into stars. Therefore, in advance of determining the SFR-related parameters, the SN feedback-related parameters must be determined by matching the local luminosity function.

Figure 4 shows the ratio of cold gas mass relative to B -band luminosity of spiral galaxies as a function of their luminosity. Theoretical result is shown only for the CSF model by the solid line. Other SF models of DSF2, DSF1 and DSF0 provide almost the same results, and their differences from the CSF are only about 0.1 dex. We here assume that 75% of the cold gas in the models is comprised of hydrogen, i.e., $M_{\text{HI}} = 0.75M_{\text{cold}}$. HI data, taken from Huchtmeier & Richter (1988), are shown by open squares with errorbars. Since their data do not include the fraction of H_2 molecules, they should be regarded as providing a lower limit to the mass fraction of cold gas. Adopted values of the parameters in the SF models are tabulated in Table 2. Slight difference in the values of τ_*^0 stems from the different redshift-dependence of SF timescale.

Figure 5 shows the effective disk radii of local spiral galaxies as a function of their luminosity only for the CSF model. Other SF models also provide almost the same results as CSF and are not shown. Thus, with the use of $(\lambda, \sigma_\lambda) = (0.03, 0.5)$, all the SF models well reproduce the observed disk size-magnitude relation (thin solid line) compiled by Totani & Yoshii (2000) based on the data taken from

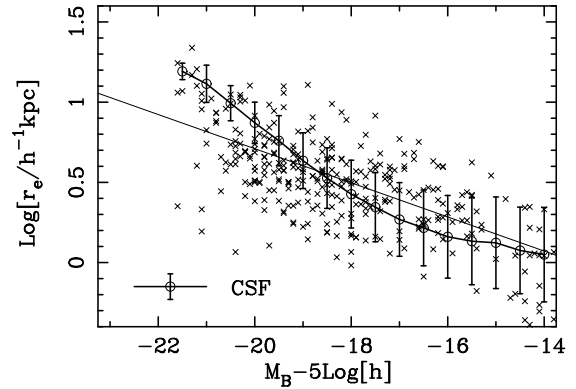


FIG. 5.— Disk size of spiral galaxies. The thick solid line connecting open circles shows the theoretical result for effective radii of spiral galaxies in the CSF model. Errorbars on this line is the 1σ scatter in predicted sizes. Other SF models, not shown, give almost the same results with less than 0.1 dex difference. The thin line indicates the mean relation given by Totani & Yoshii (2000) for spiral galaxies, based on the observational data (crosses) taken from Impey et al. (1996).

Impey et al. (1996), while showing a slightly steeper slope than the observed one.

4. RESULTS

4.1. Relationships between Size and Magnitude

First, we examine the size distribution of elliptical galaxies, because it is directly affected by the dynamical response to gas removal. Figure 6 shows the contour distribution in the effective radius versus absolute B -magnitude diagram. The levels of contours in order from outside to inside are 0.02, 0.1, 0.2, 0.3, 0.4, 0.5, 0.6, 0.7, 0.8 and 0.9 times the largest number of galaxies in grids. This way of description applies to all the contour distributions shown below. The four panels show the results for the models of CSF, DSF2, DSF1 and DSF0, respectively, as indicated. Effective radius r_e of model galaxies are defined by $0.744r_b$, where r_b is the three-dimensional half-mass radius, assuming the de Vaucouleurs profile (Nagashima & Yoshii 2003). The filled triangles and squares represent the data taken from Bender, Burstein & Faber (1992, 1993) and Mateo (1998), respectively. When some of dwarf spheroidals are listed in both their tables, we use the data in Bender, Burstein & Faber (1992, 1993). Observed elliptical galaxies have two sequences of dispersed dwarf galaxies with low surface brightness and compact dwarf galaxies with high surface brightness.

As shown in Figure 2, the CSF model has the longest SF timescale at high redshift among the four SF models. This means that when a major merger occurs in the CSF model, a significant fraction of gas is removed, so that the dynamical response of dwarf galaxies is expected to be the largest. Figure 6 clearly shows that the CSF model (*panel a*) predict many dwarf galaxies with very large size of $r_e \sim 10 - 10^2 h^{-1} \text{ kpc}$ for $M_B - 5 \log h \gtrsim -10$. In the range of $-10 \gtrsim M_B - 5 \log h \gtrsim -15$, the peak of distribution is on the sequence of dispersed dwarf ellipticals. On the other hand, the DSF0 model (*panel d*) has the shortest SF timescale at high redshift, so that the effects of gas removal are not significant. Most of galaxies are distributed along a single power-law sequence, corresponding to the compact dwarf galaxies. The slope is determined by α_{hot} as shown in Nagashima et al. (2001), in which they simply determined the size of elliptical galaxies by $GM_b/2V_b^2$. The behavior of SF timescale indicates that the models of DSF1

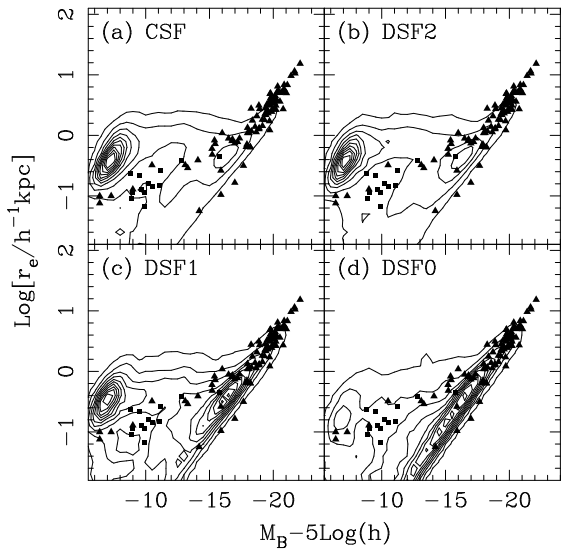


FIG. 6.— Distribution of effective radius for elliptical galaxies in the models of (a) CSF, (b) DSF2, (c) DSF1, and (d) DSF0, where the effects of dynamical response to starburst-induced gas removal are taken into account. Based on the calculated number of such galaxies per magnitude per logarithm of kpc, the levels of contours shown in order from outer to inner are 0.02, 0.1, 0.2, 0.3, 0.4, 0.5, 0.6, 0.7, 0.8, and 0.9 times the largest number of galaxies in grids, respectively. Symbols indicate the observational data given by Bender, Burstein & Faber (1992) (triangles) and Mateo (1998) (squares).

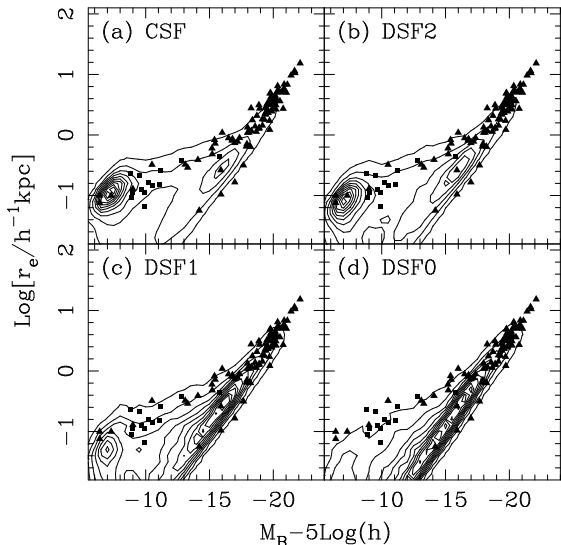


FIG. 7.— Distribution of effective radius for elliptical galaxies. Same as Figure 6, but for the SF models without the effects of dynamical response to starburst-induced gas removal.

and DSF2 are intermediate between CSF and DSF0. This suggests that the SF timescale should be constant independent of redshift or very weakly dependent on redshift, but not proportional to the dynamical timescale of galaxies.

It should be noted that the gas removal is not a unique mechanism to make large ellipticals. If a galaxy just after major merger keeps a large fraction of gas, its size becomes larger than that of gas-poor system with the same stellar mass because the size is proportional to the total mass of stars and cold gas. This can be seen directly if we do not take into account the effects of dynamical response to gas removal. Figure 7 shows the same result as Figure 6 except without the effects of dynamical response. The overall shapes are similar,

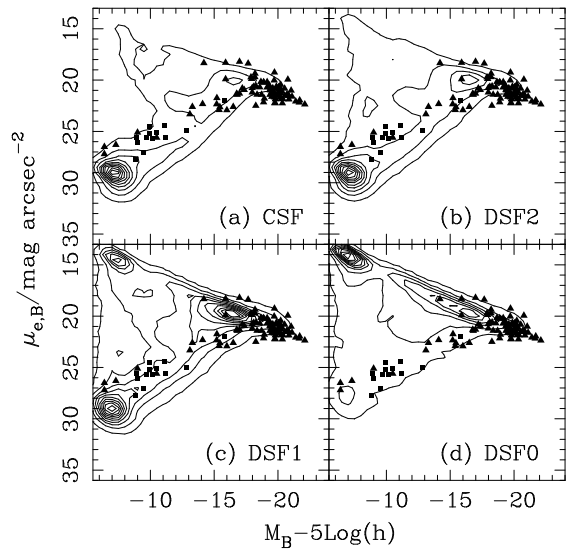


FIG. 8.— Distribution of B -band surface brightness within the effective radius for elliptical galaxies in the models of (a) CSF, (b) DSF2, (c) DSF1, and (d) DSF0, where the effects of dynamical response to starburst-induced gas removal are taken into account. Contours and symbols have the same meanings as in Figure 6.

independent of SF timescale, because the effects of dynamical response are not taken into account. However the peak locations in Figure 7 are different from those in Figure 6. This is because the mass of cold gas just after major merger determines its size as mentioned above and therefore the size depends on the SF timescale. In other words, the CSF model has a larger fraction of cold gas and hence a larger galactic mass at high redshift, compared with the DSF models. This situation without the effects of dynamical response corresponds to the case of *dominant dark halo* in Dekel & Silk (1986), in which the size and velocity dispersion do not change during the gas removal. We therefore conclude that in realistic situations the dark matter is not always dominant in the gravitational potential. Note that while the $r_e - M_B$ relation is reproduced even without the effects of the dynamical response, as will be shown in the next subsection, the Faber-Jackson relation is not reproduced unless the effects are properly taken into account (see Figures 12 and 14).

In addition to size and magnitude, surface brightness is also an important observable quantity. Two sequences of dispersed and compact dwarf galaxies are prominent in the surface brightness versus absolute B -magnitude diagram, as shown in Figure 8. Surface brightness of model galaxies is defined as the average brightness in the area encircled by effective radius. For giant ellipticals, surface brightness is predicted to become brighter towards brighter magnitude with shallow slope, converging to $\mu_{e,B} \simeq 22$, as observed. For $M_B - 5 \log h \gtrsim -18$, surface brightness widely spreads. This magnitude corresponds to V_{hot} , that is, the magnitude at which β becomes larger than unity. The CSF and DSF2 models make the widely spread distribution which reproduces two sequences simultaneously and thus are likely, while the DSF0 makes one sequence of compact ellipticals only.

In all the SF models there are many galaxies with very low surface brightness for $M_B - 5 \log h \gtrsim -15$. Actually such galaxies cannot be detected unless the detection threshold of surface brightness is faint enough in galaxy survey observations. With a cutoff of $\mu_{e,B} = 26.5$ taken into account in both

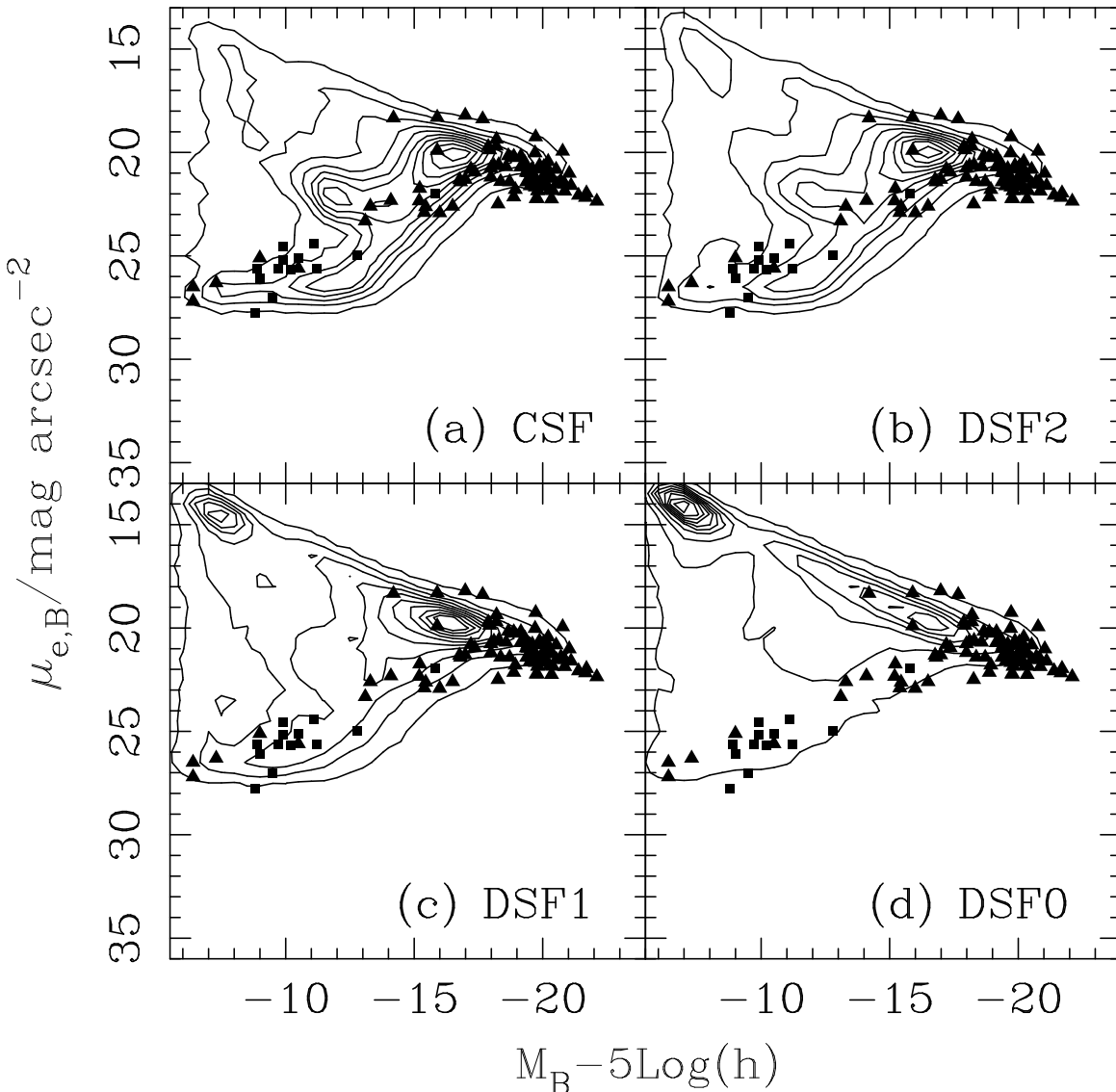


FIG. 9.— Distribution of B -band surface brightness within the effective radius for elliptical galaxies. Same as Figure 8, but for only galaxies of high surface brightness with $\mu_{e,B} \leq 26.5$ in the models as well as the data.

the model and observed data, we show the surface brightness versus absolute B -magnitude diagram in Figure 9 and the effective radius versus absolute B -magnitude diagram in Figure 10. For the models of CSF and DSF2 the resultant distributions in both of these diagrams are consistent with the data.

As another combination of observable quantities, the surface brightness versus size relation is often referred to as the Kormendy relation (Kormendy 1977). Figure 11 shows the theoretical distribution of elliptical galaxies with $\mu_{e,B} \leq 26.5$ in the surface brightness versus effective radius diagram. Extended distribution toward low surface brightness is clearly seen for the models of CSF and DSF2.

4.2. Faber-Jackson Relation

Velocity dispersion of elliptical galaxies is also an independent dynamical observable. If the dark matter dominates the baryonic matter, the velocity dispersion of galaxies reflects that of their host dark halos. On the other hand, in the case of negligible dark matter, the velocity dispersion is substantially affected by dynamical response to gas removal in proportion

to the mass fraction of removed gas. Thus the velocity dispersion versus absolute magnitude relation for elliptical galaxies, often called Faber-Jackson (FJ) relation, provides another strong constraint on galaxy formation (Faber & Jackson 1976).

Figure 12 shows the velocity dispersion versus absolute B -magnitude diagram for the models of CSF, DSF2, DSF1 and DSF0. Velocity dispersion of model galaxies is assumed to be isotropic and is converted to one-dimensional central dispersion by $\sigma_0(1D) = V_b/\sqrt{3}$ after increased to the central value by a factor of $\sqrt{2}$ according to the de Vaucouleurs-like profile. For the DSF0 model, galaxies with velocity dispersion less than 10 km s^{-1} is scarcely distributed. Note that the cutoff circular velocity V_{low} , above which dark halos are identified as isolated objects, is 30 km s^{-1} nearly corresponding to the Jeans scale for collapse after cosmic reionization (Ostriker & Gnedin 1996). This makes the sequence that converges to $\sigma_0(1D) = 30/\sqrt{3} \simeq 17 \text{ km s}^{-1}$. For the DSF0 model, we see only such sequence because the smallest fraction of

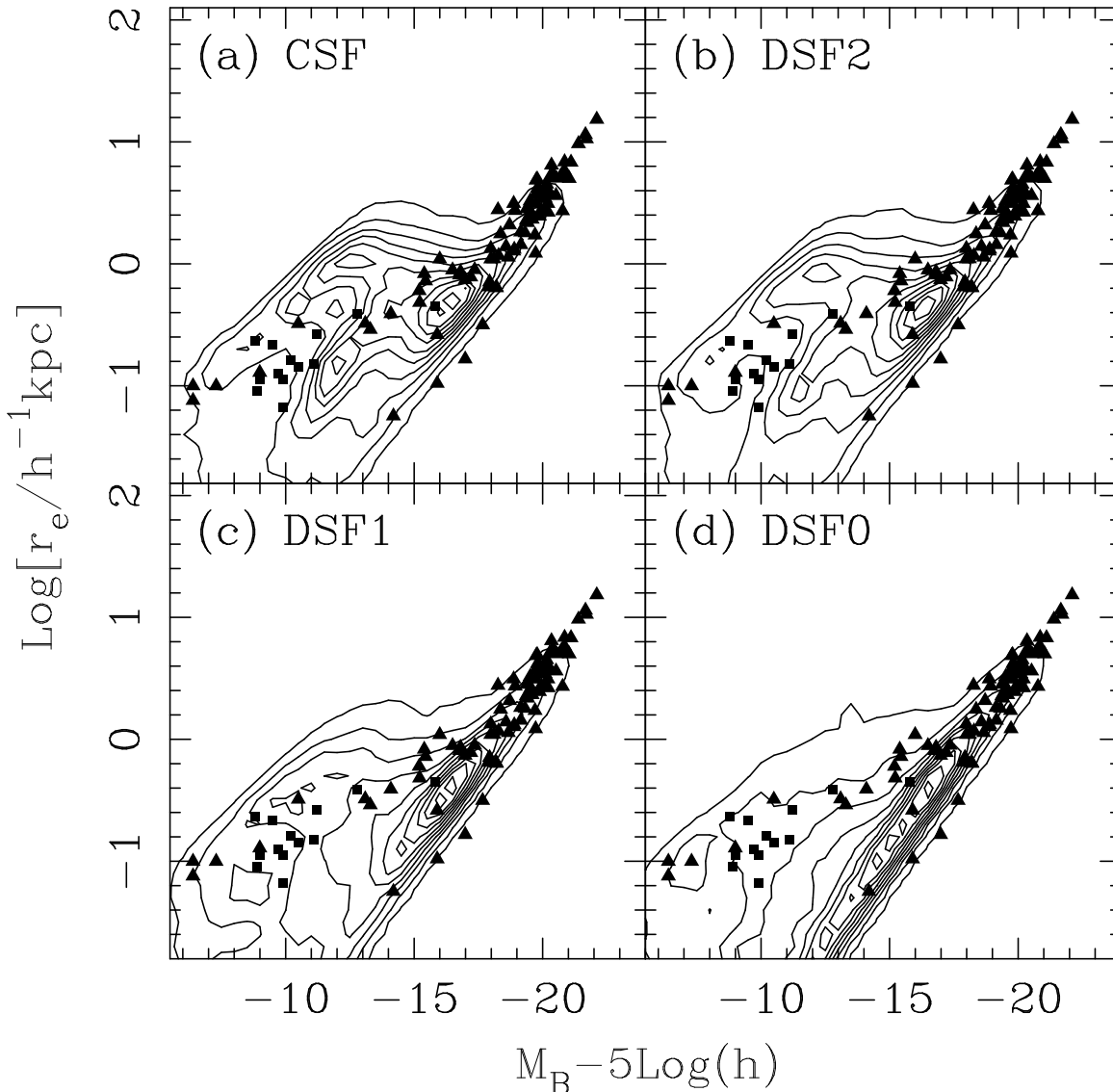


FIG. 10.— Distribution of effective radius for elliptical galaxies. Same as Figure 6, but for only galaxies of high surface brightness with $\mu_{e,B} \leq 26.5$ in the models as well as the data.

gas at major merger in this model gives very weak effects of dynamical response to gas removal. It should be noted that this tendency hardly depends on V_{low} because the SN feedback is very efficient for dwarf galaxies. In contrast, other SF models can reproduce the low velocity dispersion observed for local dwarf spheroidals for $M_B - 5 \log h \gtrsim -15$.

It is possible that dwarf galaxies with very low velocity dispersion would remain undetected from actual observations, because such galaxies are expected to have very low surface brightness as a result of dynamical expansion by gas removal. Figure 13 therefore shows the FJ relation after excluding galaxies of lower surface brightness with $\mu_{e,B} \geq 26.5$. Most of dwarf galaxies of low circular velocity are excluded from the CSF model and their distribution is in apparent disagreement with the data. This situation is a little improved for the models of DSF1 and DSF2. Figure 13 clearly indicates the difficulty of making dwarf galaxies of low circular velocity and high surface brightness. In other words, the FJ relation strongly constrains the SF timescale requiring the mild or negligible redshift dependence, when compared with the

dynamical timescale.

Here we examine the effects of the dynamical response on velocity dispersion. Figure 14 shows the velocity dispersion versus absolute B -magnitude diagram without the effects of dynamical response as in Figure 7. Evidently, all four SF models cannot reproduce the dwarf galaxies of low circular velocity and give almost the same distribution on this diagram independent of SF timescale. This highlights the importance of dynamical response for the formation of dwarf galaxies. Kauffmann & Charlot (1998) predicted the FJ relation in their SAM with no dynamical response taken into account and claimed to find good agreement with observations. Their result is, however, limited only to $M_B \lesssim -18$, where such dynamical response has no significant effect. Thus our SAM analysis is the first that has reproduced the observed velocity dispersion even for dwarf galaxies.

4.3. Mass-to-Light Ratio

The mass, which is used to estimate the mass-to-light ratio, is the dynamical mass of $M_{\text{dyn}} \propto r_b \sigma^2 / G$. In our SAM,

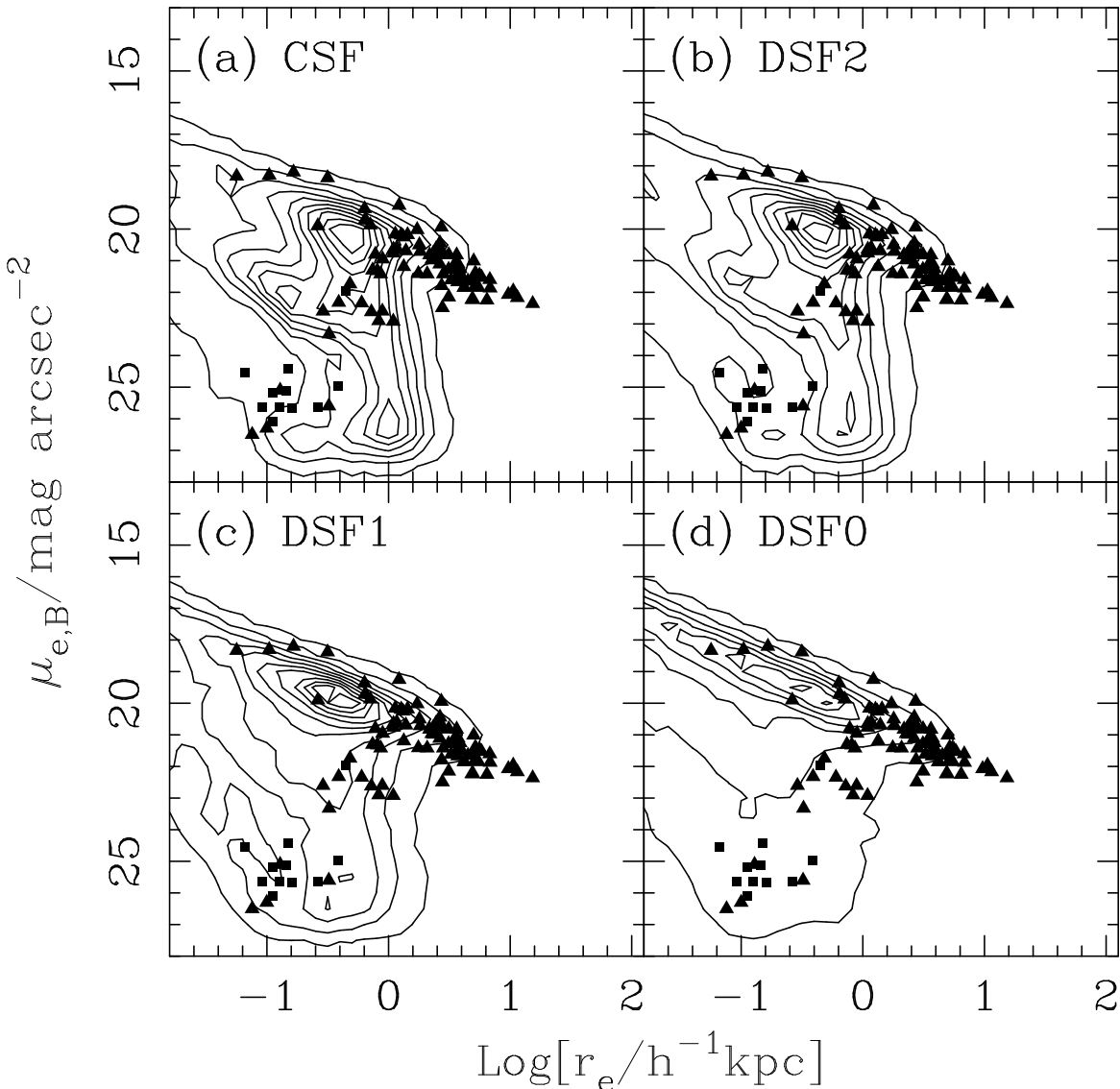


FIG. 11.— Kormendy relation for elliptical galaxies with $\mu_{e,B} \leq 26.5$ in the models of (a) CSF, (b) DSF2, (c) DSF1, and (d) DSF0, where the effects of dynamical response to starburst-induced gas removal are taken into account. Contours and symbols have the same meanings as in Figure 9.

the size r_b and the velocity dispersion σ are determined by the amount of baryonic matter that escapes out of the system against the underlying dark matter potential. In this paper we define the dynamical mass by $M_{\text{dyn}} = 2r_b V_b^2 / G$. Figure 15 shows the mass-to-light ratio of elliptical galaxies as a function of absolute B -magnitude for the four SF models.

Our SAM well reproduces the observed mass-to-light ratio for giant ellipticals, and at least qualitatively the mass-to-light ratio for dwarf spheroidals that increases towards faint magnitude. As for giant ellipticals, observed data still have a large scatter. This might be caused by an uncertainty in estimating dynamical mass owing to anisotropic kinematics and rotation.

Such trend of the mass-to-light ratio for dwarf spheroidals is not caused by the dynamical response alone. Figure 16 shows the mass-to-light ratio with no dynamical response taken into account, which turns out to be very similar to or slightly higher than that with dynamical response in Figure 15. Therefore, considerably high values up to $M/L_B \sim 10^3$ are caused by the dominant dark halo in which the size and velocity dispersion are kept unchanged during the starburst.

Since the luminosity L_B is proportional to the final mass M_f , it follows that $M/L_B \propto M_i/M_f \propto \beta$ in the limit of $\beta \gg 1$, where β measures the strength of the SN feedback in equation (9). Using a relation $M \propto V_{\text{circ}}^3$ from the spherical collapse model (Tomita 1969; Gunn & Gott 1972), we obtain

$$\frac{M}{L_B} \propto \beta \propto \sigma_i^{-\alpha_{\text{hot}}} \propto M_f^{-\alpha_{\text{hot}}/(3+\alpha_{\text{hot}})}. \quad (20)$$

If we adopt $\alpha_{\text{hot}} = 4$, then $M/L_B \propto M_f^{-4/7} \propto 10^{8M_B/35}$. The slope of this relation explains the result in Figure 16. Therefore, the smaller mass fraction of dark matter lowers the mass-to-light ratio (Dekel & Silk 1986; Yoshii & Arimoto 1987). In apparent contrast to this, the DSF0 model scarcely forms galaxies of such high mass-to-light ratio. This is because the size is determined by the baryonic mass, $r_e \propto GM_b/V_b^2$, and because the removed gas is negligible due to the short SF timescale at high redshift.

By excluding galaxies of lower surface brightness with $\mu_{e,B} \geq 26.5$, we obtain gross agreement with the observed mass-to-light ratio in Figure 17.

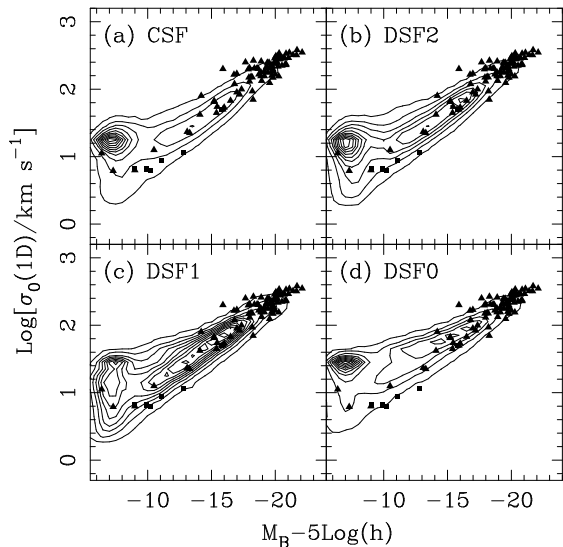


FIG. 12.— Faber-Jackson relation for elliptical galaxies in the models of (a) CSF, (b) DSF2, (c) DSF1, and (d) DSF0, where the effects of dynamical response to starburst-induced gas removal are taken into account. One-dimensional central velocity dispersion $\sigma_0(1D)$ for model galaxies is estimated from $V_b/\sqrt{3}$ after increased to the central value by a factor of $\sqrt{2}$ according to the de Vaucouleurs-like profile. Contours and symbols have the same meanings as in Figure 6.

4.4. Metallicity-Magnitude Relation

Figure 18 shows the mean stellar metallicity as a function of absolute B -magnitude for elliptical galaxies. The vertical axis represents the logarithmic iron abundance $[\text{Fe}/\text{H}]$. Shown by symbols are the data compiled by Mateo (1998) and those translated from Mg_2 index for those taken by Bender, Burstein & Faber (1993), whereas by contours the L_B -weighted average of logarithmic metal abundances of stars $\langle \log(Z_*/Z_\odot) \rangle_{L_B}$ for the theoretical prediction. Since the theoretical results are almost independent of whether galaxies of low surface brightness are excluded, we only show the metallicity distribution excluding such galaxies with $\mu_{e,B} \geq 26.5$. We do not show the metallicity distribution for spirals, which is similar to that for ellipticals.

All the SF models well reproduce the observed tight relation between metallicity and absolute magnitude. This means that such relation is not affected by the redshift dependence of SF timescale, because we adopt the SN feedback in the same way irrespective of either continuous or burst formation of stars in galaxies. With strong SN feedback with $\alpha_{\text{hot}} \simeq 4$, our SAM succeeds to explain the observed low metallicity $[\text{Fe}/\text{H}] \sim -2$ at $M_B - 5 \log h \simeq -10$, in spite of using a rather high value of metallicity yield $y = 2Z_\odot$. Note that if $\alpha_{\text{hot}} = 2$, we obtain about a factor of three higher metallicity at that magnitude. This is consistent with the conclusion by Cole et al. (2000) that with $\alpha_{\text{hot}} = 2$ the metallicities of their dwarf galaxies are systematically higher than the data, while such predicted values reside in a range of large observed scatter.

5. CONSISTENCY WITH OTHER OBSERVATIONS

In this section, we show the whole aspects of our SAM to check the consistency with other local and high-redshift observations. This will clarify the limitations of present SAM analyses and physical processes for which further investigation is required. In the first three subsections (§§5.1-5.3),

high-redshift properties of model galaxies are examined by comparing the observed galaxies in the Hubble Deep Field (HDF, Williams et al. 1996) and the Subaru Deep Field (SDF, Maihara et al. 2001). Then, the Tully-Fisher relation (TFR) for local spiral galaxies (§5.4) and the color-magnitude relation (CMR) for cluster elliptical galaxies (§5.5) are discussed.

5.1. Faint Galaxy Number Counts

Counting galaxies as a function of apparent magnitude is one of the most important observable quantities for constraining the geometry of the universe and the evolution of galaxies (e.g., Yoshii & Takahara 1988). We already showed that our SAM can simultaneously reproduce the UV/optical galaxy counts in the HDF (Nagashima et al. 2001) and the near-infrared galaxy counts in the SDF (Nagashima et al. 2002). These previous works demonstrated that inclusion of the selection effects arising from the cosmological dimming of surface brightness of high-redshift galaxies derived by Yoshii (1993) is essential, because the number count of galaxies is obtained by summing up the product of luminosity function and cosmological volume element to the accessible maximal redshift above which galaxies have the surface brightness fainter than the threshold and thus are not detected. Details of the method to estimate such selection effects are found in Yoshii (1993), Totani & Yoshii (2000), Totani et al. (2001) and Nagashima et al. (2001, 2002).

In this paper the YNY mass function of dark halos (§2.1) is used instead of the PS, and the dynamical response to gas removal is a novel ingredient in the analysis. With these modifications we reexamine the galaxy counts again. Figure 19 shows the UV/optical galaxy counts in the HDF ($U_{300}, B_{450}, V_{606}$ and I_{814} in the AB system). For reference, other ground-based observed counts are also plotted. The thick solid and dashed lines show the predictions of CSF and DSF2, respectively, taking into account the absorption by internal dust (Totani & Yoshii 2000) and by intervening H I clouds (Yoshii & Peterson 1994), and the selection effects due to cosmological dimming of surface brightness (Yoshii 1993). We adopt $\rho = 1$ in equation (11), which determines the disk size at high redshift. The thin lines represent the same models, except without the selection effects. We do not show the models of DSF1 and DSF0, because they are much the same as CSF and DSF2 with only small difference comparable to observational errors. These models only slightly underpredict the U_{300} count and overpredict the I_{814} count, as pointed out by Nagashima et al. (2001).

Figure 20 shows the near-infrared galaxy counts in the SDF (K'). Like the HDF counts, the models of CSF and DSF2 well reproduce the SDF counts. For the purpose of comparison, the DSF0 model is also shown. Because of the highest SFR at high redshift, the stellar mass in this model increases rapidly, making too many faint galaxies to reproduce the observation. Therefore, the models of CSF and DSF2 give the predictions that agree with the HDF and SDF counts simultaneously.

5.2. Redshift Distribution

Figure 21 shows the redshift distributions of I_{814} -selected galaxies in the HDF with $22 \leq I_{814} \leq 24$ (panel a), $24 \leq I_{814} \leq 26$ (panel b) and $26 \leq I_{814} \leq 28$ (panel c). The number of model galaxies in each panel is calculated over the same celestial area as the HDF. The thick solid, dashed and dot-dashed lines show the results of CSF, CSF with $\sigma_8 = 1$ and DSF0, respectively. The histogram in each panel is the observed photometric redshift distribution by Furusawa et al.

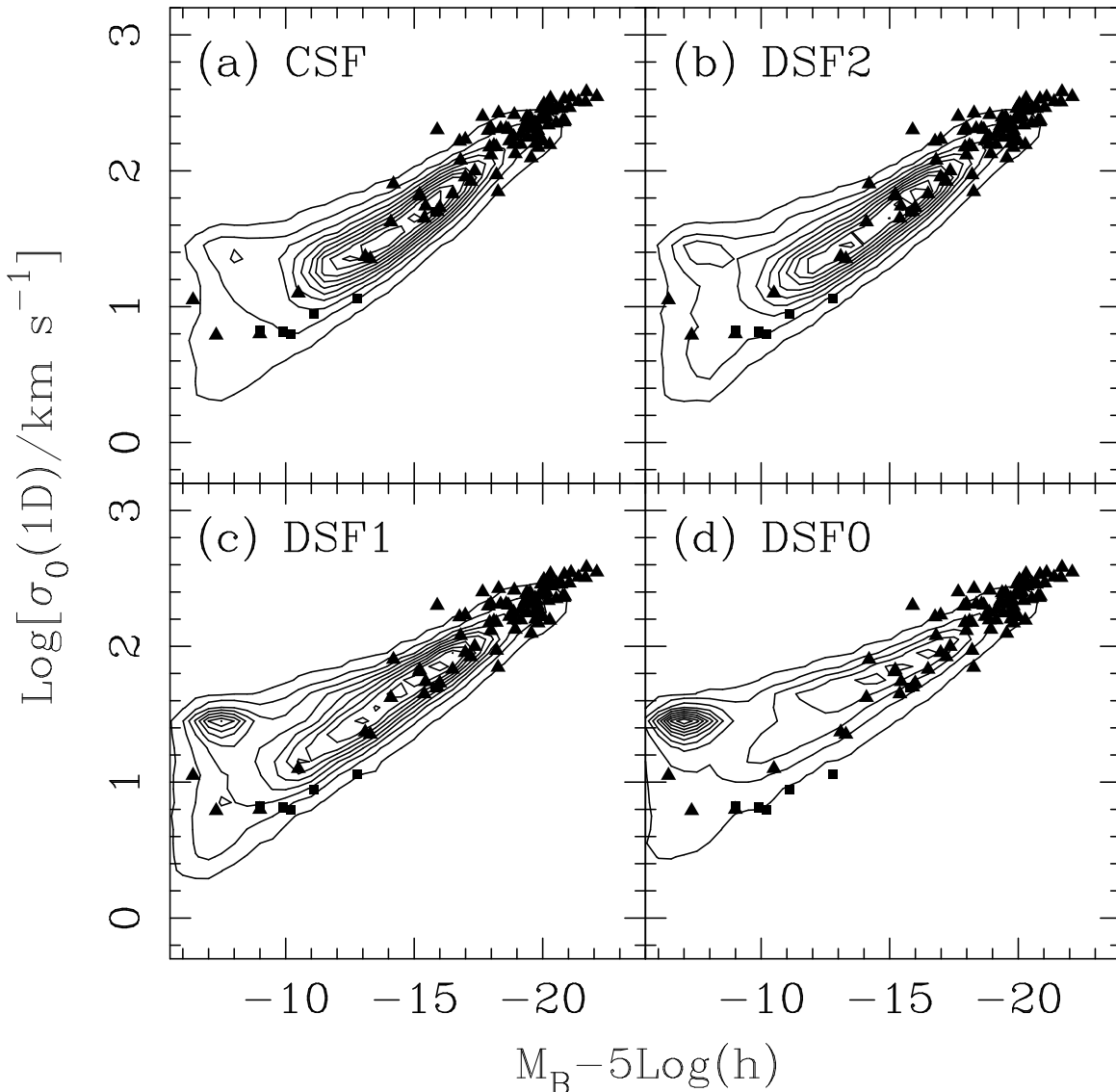


FIG. 13.— Faber-Jackson relation for elliptical galaxies. Same as Figure 12, but for only galaxies of high surface brightness with $\mu_{e,B} \leq 26.5$ in the models as well as the data.

(2000), in which they improved the redshift estimation over Fernández-Soto, Lanzetta & Yahil (1999). The difference between the results of CSF and DSF0 is very small for bright galaxies with $I_{814} \leq 26$ (panels *a* and *b*). While the CSF model reproduces the observed redshift distribution over an entire range of apparent I_{814} -magnitudes considered, the DSF0 model predicts too many high-redshift galaxies for $I_{814} \geq 26$ (panel *c*), especially at $z \gtrsim 3$. This is because the shorter SF timescale in the DSF0 model induces earlier formation of galaxies compared with CSF. These results are consistent with our previous results. We show the same model as CSF but for $\sigma_8 = 1$. Since the formation epoch of dark halos shifts to higher redshift, a little more galaxies are formed at higher redshifts. We also find that the DSF2 model reproduces the observed redshift distribution with negligible difference from the CSF model with $\sigma_8 = 1$.

5.3. Isophotal Area-Magnitude Relation

Figure 22 shows the isophotal area of galaxies plotted against their K' -magnitude, for which the same observational

condition employed in the SDF survey is used to calculate the isophoto in the SF models. The solid line indicates the mean relation with errorbars of 1σ scatter, predicted by the CSF model. Results of other SF models are almost the same, and are not shown. The data plotted by the crosses are those for the SDF galaxies that are detected in both the K' - and J -bands. As stressed in our previous papers, the selection effects from the cosmological dimming of surface brightness of galaxies cannot be ignored in the SAM analysis of galaxy number counts. This indicates that the size of high-redshift galaxies must be modeled properly.

With the selection effects correctly taken into account, the predicted size should converge towards the limiting magnitude, because faint galaxies with larger area have surface brightnesses below the detection threshold and then remain undetected. We find from this figure that our SAM galaxies well reproduce the observed area-magnitude relation, and are consistent with the SDF galaxies, only when the selection bias against faint galaxies with high redshift and/or low surface brightness is taken into account in the analysis.

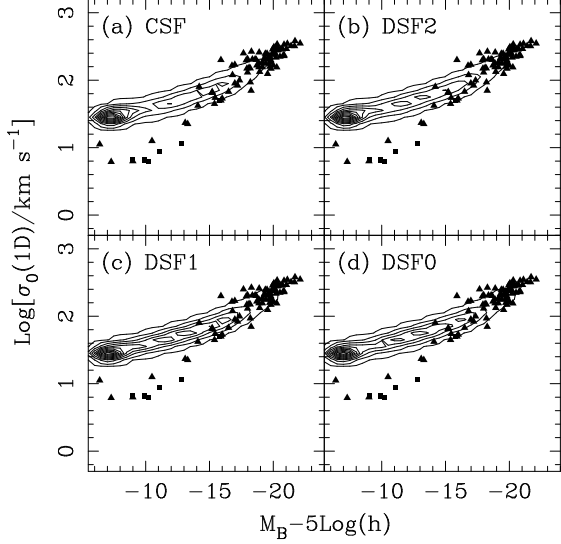


FIG. 14.— Faber-Jackson relation for elliptical galaxies. Same as Figure 12, but for the SF models without the effects of dynamical response to starburst-induced gas removal.

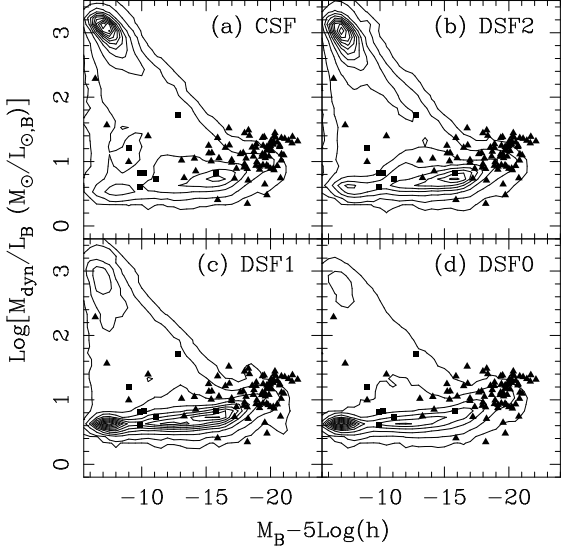


FIG. 15.— Distribution of B -band mass-to-light ratio for elliptical galaxies for the models of (a) CSF, (b) DSF2, (c) DSF1, and (d) DSF0, where the effects of dynamical response to starburst-induced gas removal are taken into account. Contours and symbols have the same meanings as in Figure 12, but for the outermost contour level added showing 10^{-3} times the largest number of galaxies in grids.

5.4. Tully-Fisher Relation (TFR)

Figure 23 shows the I -band TFR. The thick solid line indicates the predicted TFR with errorbars of 1σ scatter for gas-rich spirals in the CSF model, having more than 10% mass fraction of cold gas in the total galactic mass, that is, $M_{\text{cold}}/(M_* + M_{\text{cold}}) \geq 0.1$. This criterion is the same as that used by Cole et al. (2000). The thick dashed line is for all spirals. The tendency that gas-rich spirals for a given magnitude are always brighter than gas-poor spirals has already been shown in Cole et al. (2000). Results of other SF models are not shown because of negligible difference.

The thin dashed, dot-dashed and dotted lines are the best-fit results to the observed TFRs by Mathewson, Ford & Buchhorn (1992), Pierce & Tully

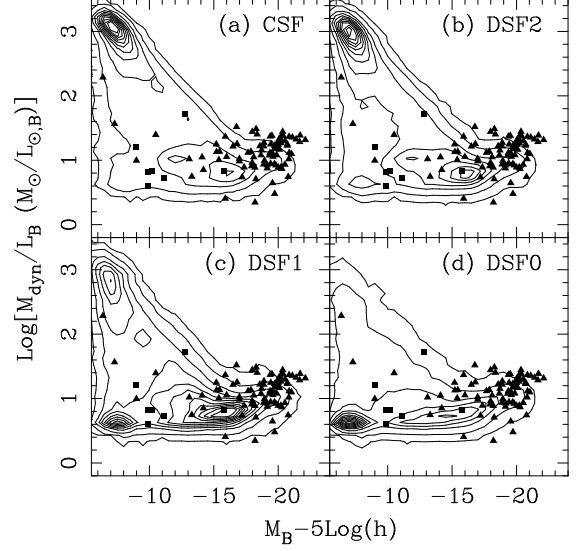


FIG. 16.— Distribution of B -band mass-to-light ratio for elliptical galaxies. Same as Figure 15, but for the SF models without effects of dynamical response to starburst-induced gas removal.

(1992), and Giovanelli et al. (1997), respectively. We assume that the line-width W is simply twice the disk rotation velocity V_{rot} as usual. For model galaxies, we set V_d to be equal to V_{rot} , as mentioned in §2.5.

The predicted TFR slope for galaxies with small rotation velocity $V_{\text{rot}} \lesssim 80\text{km}$ is steeper than that observed, while the predicted slope and magnitude for galaxies with larger velocity agree well with the observations. The TFR slope is determined by α_{hot} , because this parameter relates the mass fraction of stars in each galaxy, which gives luminosity, to the rotation velocity. We use $\alpha_{\text{hot}} = 4$ throughout as a standard, but smaller α_{hot} gives shallower slope. For the purpose of comparison, we also plot the CSF model with $\alpha_{\text{hot}} = 2$ by the dot-dashed line. In this case the slope becomes closer to that observed. Although Cole et al. (2000) adopted $\alpha_{\text{hot}} = 2$ and claimed agreement of their model with the observed TFRs, we found that this model predicts too many high-redshift galaxies to be reconciled with the observed number counts. Moreover, mean metallicity of stars in dwarf spheroidals is too high to be consistent with their observed metallicities, as shown in §4.4. In order to reproduce both observations, it might be worth relaxing our assumptions in estimating the disk rotation velocity and/or other physical processes such as SN feedback. For example, the SN feedback parameter β , which is assumed to be constant, might depend on whether star formation is either continuous or burst-like. Furthermore, it might evolve with redshift. Dynamical response to gas removal, of course, provides a promising effect on disk rotation velocity. These possibilities should therefore be investigated in more detail.

5.5. Color-Magnitude Relation (CMR)

Figure 24 shows the $V-K$ color versus magnitude relation of cluster elliptical galaxies embedded in extended dark halo with $V_{\text{circ}} = 10^3\text{km s}^{-1}$. The thick solid, dashed, dot-dashed, and dotted lines represent the predicted CMRs in the SF models of CSF, DSF2, DSF1, and DSF0, respectively. The CMR for each model is obtained by averaging 50 realizations. Errorbars to the CMR denote the 1σ uncertainties in the DSF2 model, which are comparable to CSF and DSF1 but is slightly larger than DSF0. The thin dashed line is the observed CMR

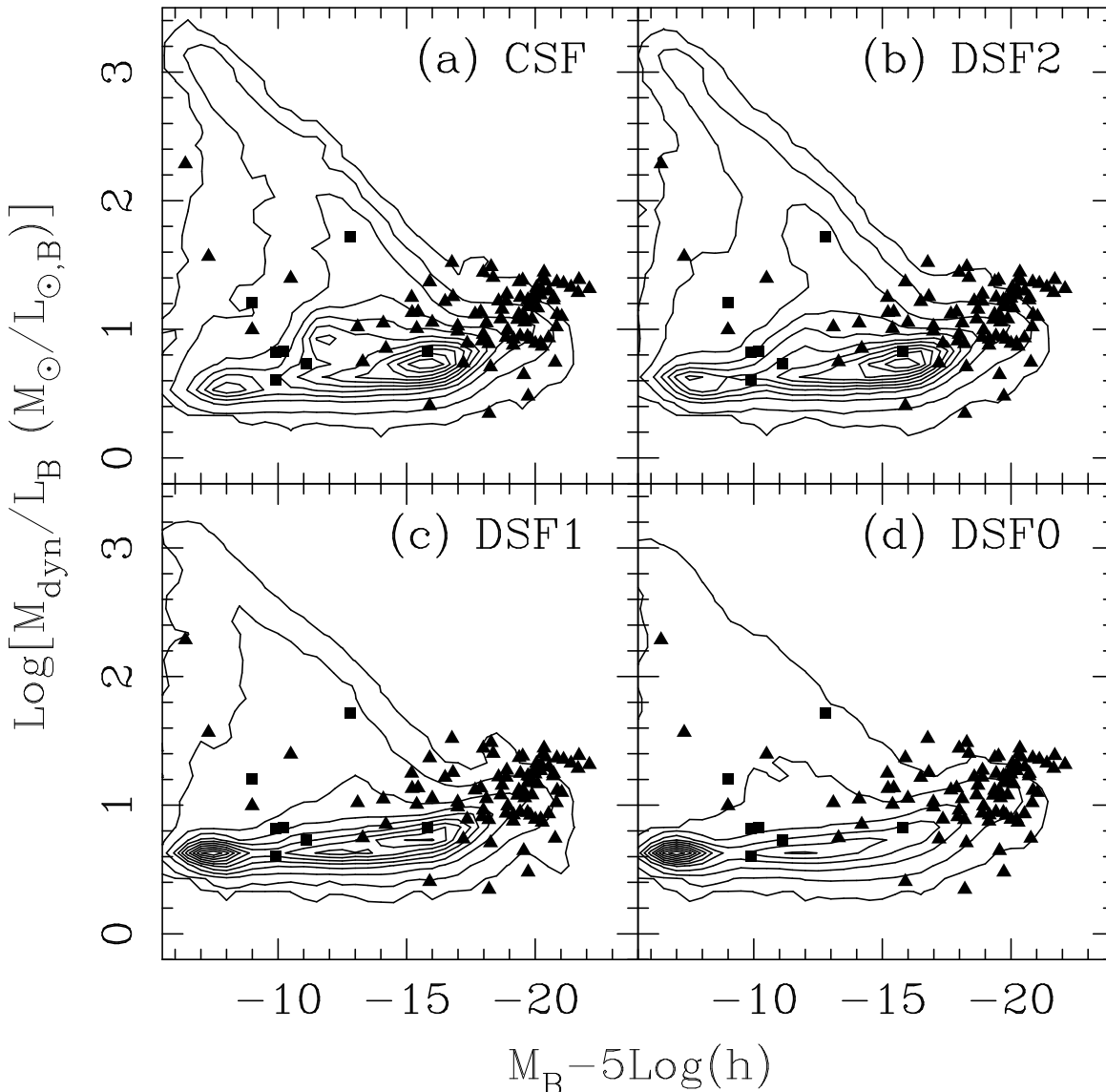


FIG. 17.— Distribution of B -band mass-to-light ratio for elliptical galaxies. Same as Figure 15, but for only galaxies of high surface brightness with $\mu_{e,B} \leq 26.5$ in the models as well as the data.

for galaxies in the Coma cluster by Bower, Lucey & Ellis (1992) and the thin solid line is the same but for the aperture-corrected CMR by Kodama et al. (1998).

All the SF models are not reconciled with the observed CMR, although the colors at $M_V - 5 \log h \simeq -20$ are consistent with the observation. This is a consequence of adopting the SN feedback with $(\alpha_{\text{hot}}, V_{\text{hot}}) = (4, 180 \text{ km s}^{-1})$, together with the satellite-satellite merger. As discussed by Kauffmann & Charlot (1998) and Nagashima & Gouda (2001), a combination of smaller $\alpha_{\text{hot}} (\simeq 2)$ and larger V_{hot} is known to give a better fit to the observed CMR.

Like the TFR, the faint-end slope of the CMR is determined by α_{hot} , because the CMR is primarily a metallicity sequence (Kodama & Arimoto 1997) and chemical enrichment of dwarf galaxies is determined by α_{hot} . The bright-end slope of the CMR is nearly flat, because the SN feedback becomes negligible. If we adopt a large value of $V_{\text{hot}} \simeq 280 \text{ km s}^{-1}$, this flat region moves brightwards. Thereby, an expected slope from α_{hot} is realized over an almost entire range of magni-

tudes. Additionally, the satellite-satellite merger makes dwarf spheroidal galaxies brighter, while keeping their color unchanged. This shifts the CMR bluewards when seen at faint magnitudes.

With these considerations, we can improve the fit to the observed CMR by adjusting the SN feedback-related parameters $(\alpha_{\text{hot}}, V_{\text{hot}})$, and the merger-related parameter f_{mrg} . However, appropriate choice of their values that could explain the observed CMR seems to invalidate other successes of our SAM. This difficulty is clearly the area of future investigation.

Furthermore, we find that a bright portion of the CMR is also affected by the cooling cutoff V_{cut} . Figure 25 shows the V_{cut} -dependence of CMR. The solid and dashed lines represent the CSF model with $V_{\text{cut}} = 250$ and 300 km s^{-1} , respectively. The dot-dashed and dotted lines are the same but for the DSF0 model. If we adopt larger V_{cut} , the metallicity becomes larger because chemical enrichment continues until lower redshift. Note that the difference between the models of CSF and DSF0 is caused mainly by the difference of mean

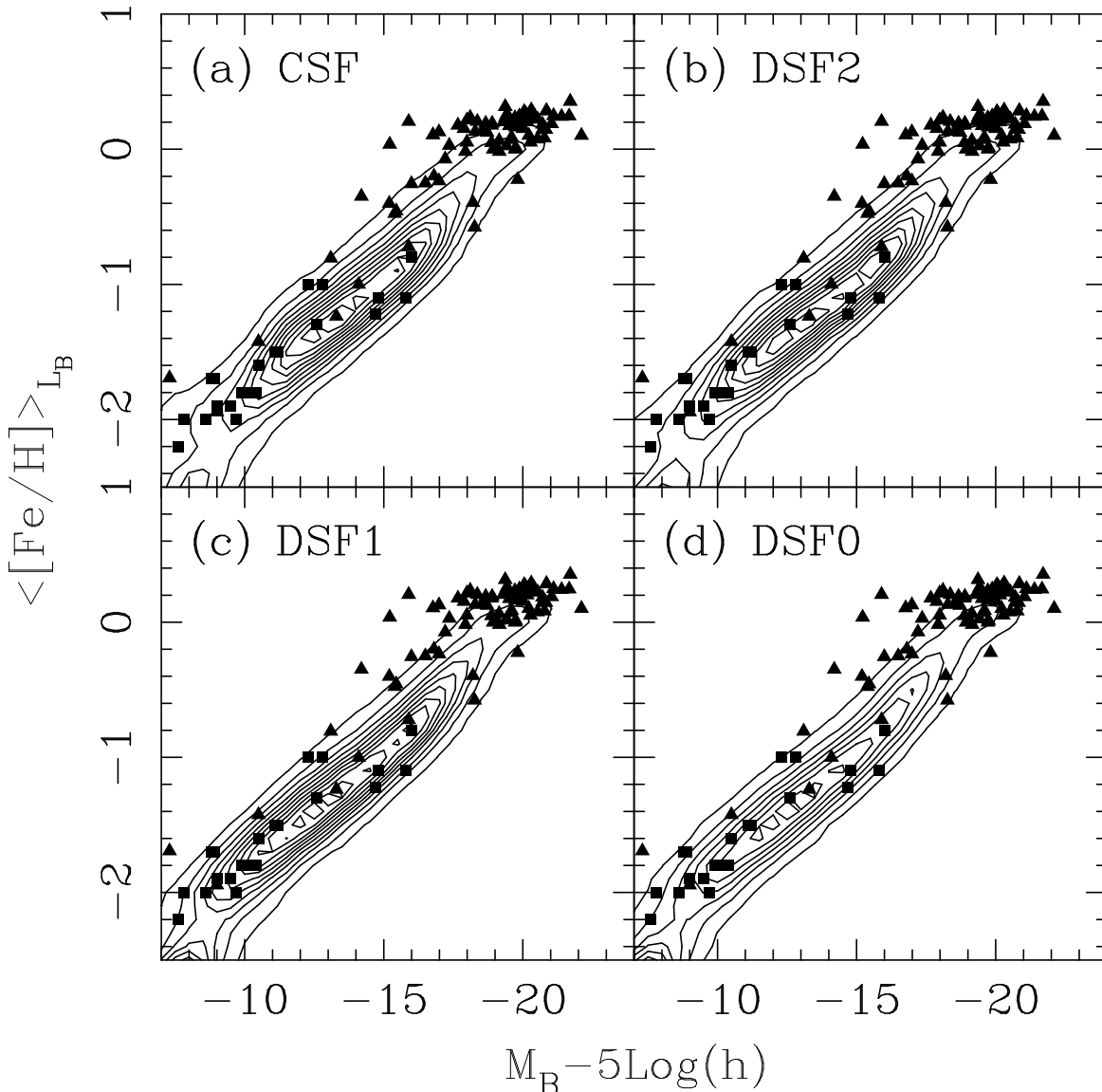


FIG. 18.— Distribution of mean stellar metallicity for elliptical galaxies in the models of (a) CSF, (b) DSF2, (c) DSF1, and (d) DSF0, where the effects of dynamical response to starburst-induced gas removal are taken into account. Contours and symbols have the same meanings as in Figure 9. Only galaxies of high surface brightness with $\mu_{e,B} \leq 26.5$ are shown, because the theoretical results in this figure are not sensitive to this threshold. The logarithmic iron abundance $[\text{Fe}/\text{H}]$ is used for the data compiled by Mateo (1998) and those translated from Mg_2 index by Bender, Burstein & Faber (1993), whereas the L_B -weighted average of logarithmic metal abundances of stars $\langle \log(Z_*/Z_\odot) \rangle_{L_B}$ for model galaxies.

stellar age, that is, stars in the DSF0 model were born earlier and thus older than CSF. Since the CMR is sensitive to V_{cut} , more knowledge of the gas cooling is needed to fix the cutoff on cluster scales.

This situation might be improved by taking the following procedures. First is to use a lower value of σ_8 below unity as recent observations suggest $\sigma_8 \simeq 0.8$ (e.g., Spergel et al. 2003). This value provides a statistically late epoch for density fluctuations to collapse. Therefore, a large value of V_{cut} does not result in the formation of monster galaxies. Second is the aperture effects. Kawata & Gibson (2003) showed the importance of aperture effects by using their chemo-dynamical simulations. The predicted $V-K$ colors of their giant elliptical galaxies are on the average 3.2 at $M_V - 5 \log h \simeq -22$ and agree well with the observed colors within 5 kpc aperture. However, the observed $V-K$ color within 99 kpc aperture is nearly equal to 3.0, which is even bluer than our predicted color at

the same magnitude. Third is the effects of UV background. Nagashima & Gouda (2001) showed that the photoionization by the UV background has a similar effect to the SN feedback. Therefore, introduction of the photoionization is equivalent to adopting larger V_{hot} . Further investigation on the CMR as well as the TFR are needed along these lines.

It should be noted that Okamoto & Nagashima (2003) have successfully reproduced the CMR slope by using a SAM combined with an N -body simulation. Their SF model corresponds to CSF with $\alpha_{\text{hot}} = 2$ and $V_{\text{hot}} = 200 \text{ km s}^{-1}$. As explained above, however, adopting this small value of α_{hot} fails to explain other observations unless the merger strength is adjusted. In this sense, high resolution N -body simulations is highly awaited to follow a full trace of merging histories of progenitor halos of clusters.

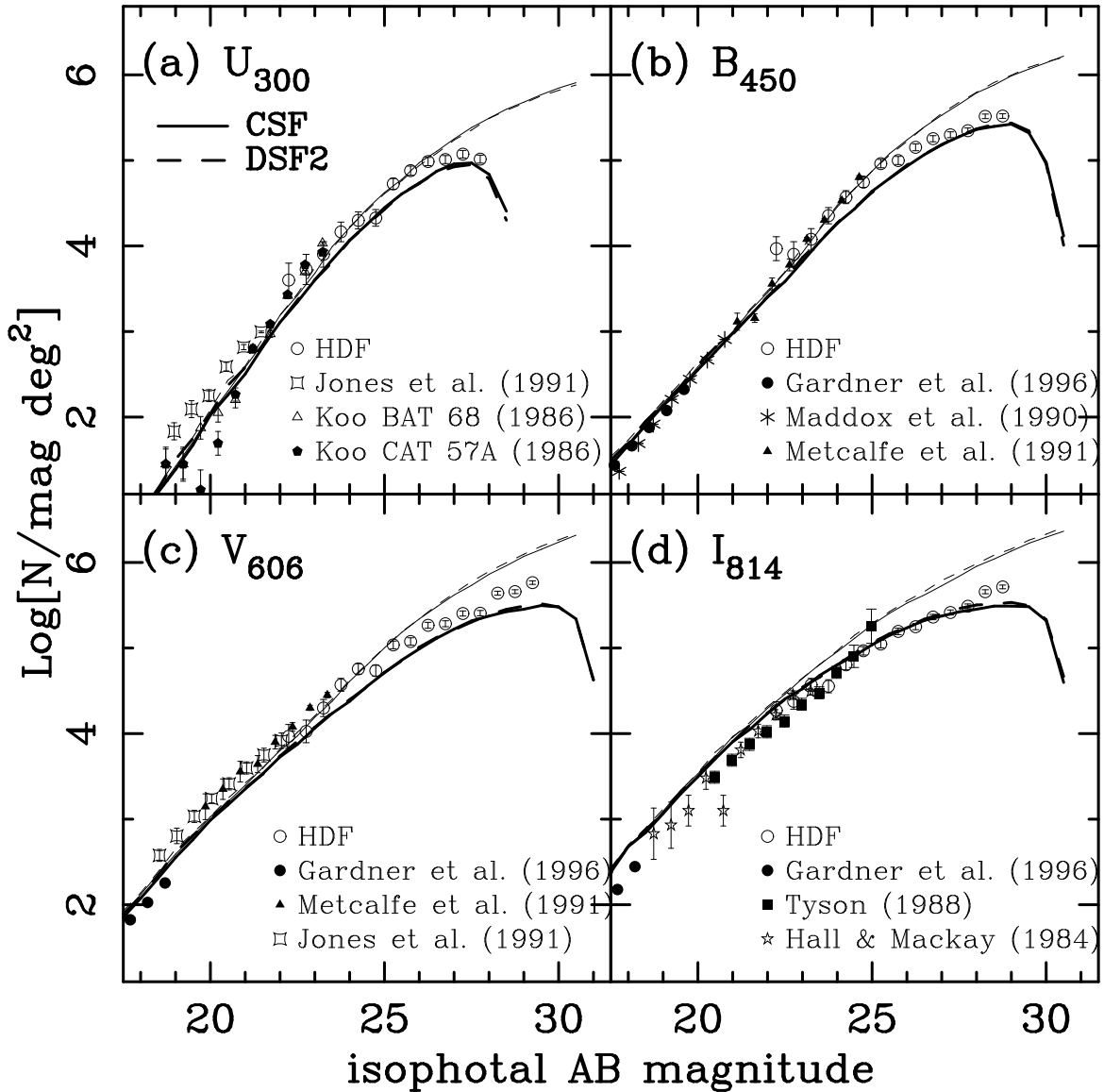


FIG. 19.— Galaxy number counts in the (a) U_{300} , (b) B_{450} , (c) V_{606} and (d) I_{814} bands, respectively. The thick and thin lines represent the SF models with and without the selection effects, respectively, arising from the same detection threshold of surface brightness of galaxies as employed in the HDF survey. For each of the cases, the solid and dashed lines represent the models of CSF and DSF2, respectively, where the effects of dynamical response to starburst-induced gas removal are taken into account. Open circles with errorbars indicate the observed HDF counts. Other symbols are ground-based observed counts.

Recently the cosmic SF history, which is a plot of SFR in a comoving volume against redshift, is widely used to examine the global SF history (Madau et al. 1996) and also in SAM analyses (Baugh et al. 1998; Somerville, Primack & Faber 2001). Since the SFR is very sensitive to the SF timescale, in Figure 26 we plot the redshift evolution of cosmic SF rate for the four models with different SF timescales. Thick lines denote the total SFR and thin lines the SFR only for starburst. Symbols with errorbars indicate observational SFRs compiled by Ascasibar et al. (2002). While there are large scatters between individual data points, the CSF and DSF2 models broadly agree with the observations.

As expected from the redshift dependence of SF timescale, the CSF model predicts a maximum SFR at relatively low redshift, $z \lesssim 2$, and the redshift at which this maximum occurs becomes larger, in order from DSF2 (dashed line) via DSF1 (dot-dashed line) to DSF0 (dotted line) as the SF timescale becomes shorter at high redshift (see Figure 2).

The fraction of cold gas available for starburst becomes larger for longer SF timescale at high redshift. Because of the same reason as above, the CSF model by the thin solid line gives the largest fraction of cold gas at major merger and therefore the highest SFR for starburst among the four models under consideration. Accordingly, the dynamical response is the most effective in the CSF model.

7. COOLING DIAGRAM REVISITED

Silk (1977) and Rees & Ostriker (1977) proposed the so-called cooling diagram, that is, the distribution of galaxies on the density versus temperature diagram. Since then, a number of authors used this diagram as crucial constraints on the formation of galaxies in the framework of monolithic cloud collapse scenario (e.g., Faber 1982; Blumenthal et al. 1984). For example, characteristic mass of galaxies can be evaluated, because the evolutionary path of gas clouds in this diagram gives an initial condition of density and temperature expected

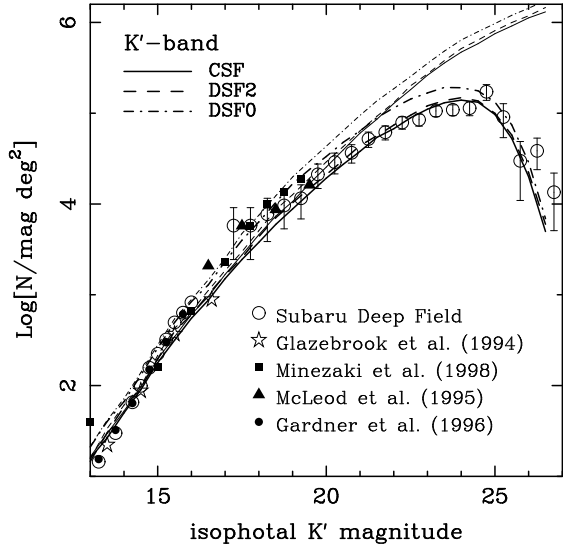


FIG. 20.— Galaxy number counts in the K' ($2.13\mu\text{m}$) band. Same as Figure 19, but for the near-infrared counts in the SDF. In addition to the models of CSF (solid lines) and DSF2 (dashed lines), the results of the DSF0 model (dot-dashed lines) are shown for comparison.

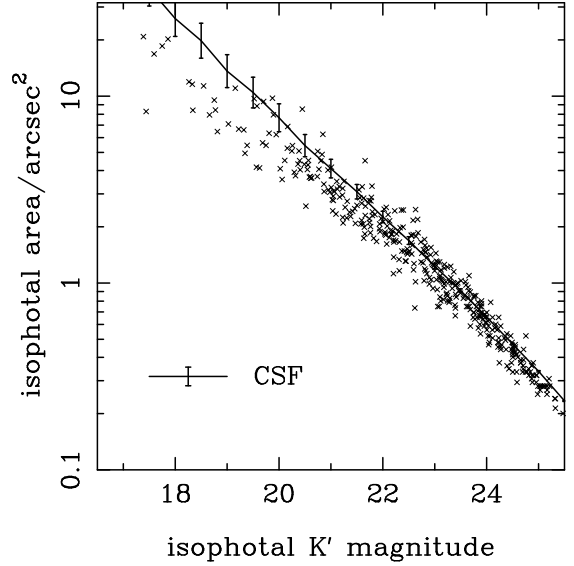


FIG. 22.— Isophotal area of the SDF galaxies against K' -magnitude. The solid line indicates the the mean relation with errorbars of 1σ scatter, predicted by the CSF model, where the effects of dynamical response to starburst-induced gas removal are taken into account. The isophoto in this model is calculated from the observational condition employed in the SDF survey. The crosses indicate the observational data from the SDF survey.

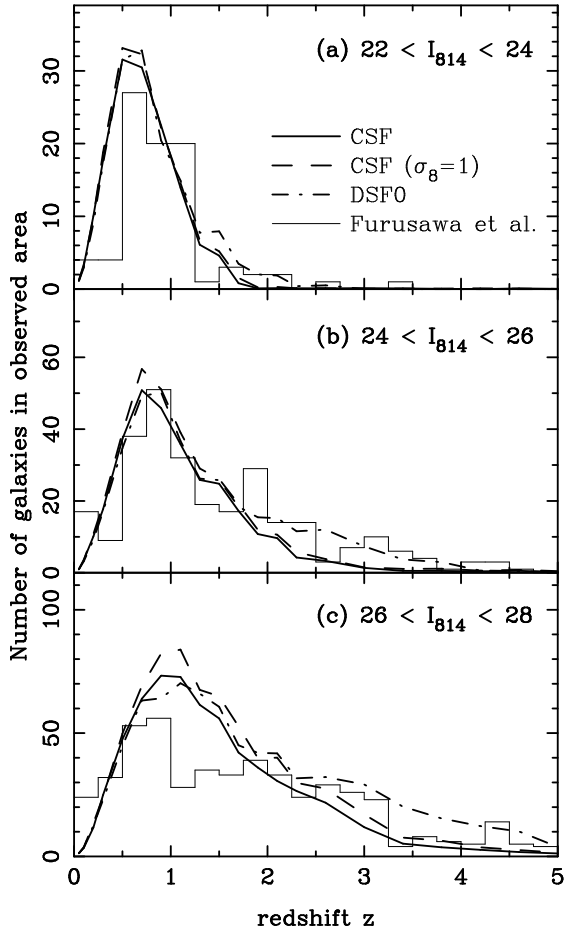


FIG. 21.— Redshift distribution of the HDF galaxies for (a) $22 \leq I_{814} \leq 24$, (b) $24 \leq I_{814} \leq 26$, and (c) $26 \leq I_{814} \leq 28$. The thick solid, dashed and dot-dashed lines represent the models of CSF, CSF with $\sigma_8 = 1$ and DSF0, respectively, where the effects of dynamical response to starburst-induced gas removal are taken into account. The histogram in each panel is the observed photometric redshift distribution by Furusawa et al. (2000).

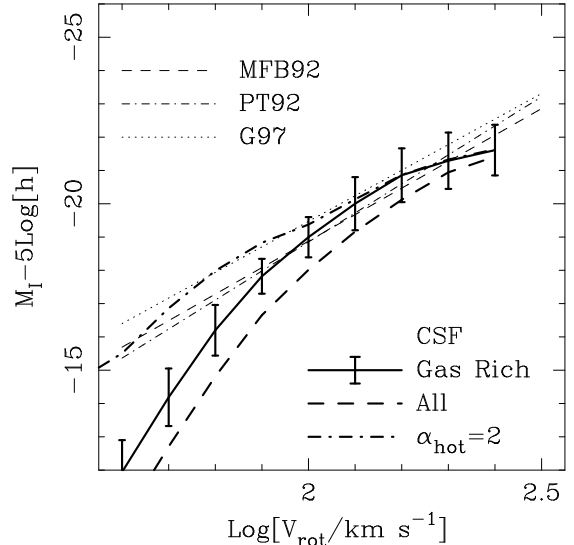


FIG. 23.— I -band Tully-Fisher relation of spiral galaxies. Variants of the CSF model with the effects of dynamical response are shown for the cases of only gas rich spirals having the cold gas more than 10% in mass (thick solid line), all spirals with our standard set of parameters (thick dashed line), and gas rich spirals with a smaller value of $\alpha_{\text{hot}} = 2$ (thick dot-dashed line). Errorbars indicate 1σ scatter around the predicted mean. The observed TFRs are shown as a mean relation given by Mathewson, Ford & Buchhorn (1992) (thin dashed line), Pierce & Tully (1992) (thin dot-dashed line), and Giovanelli et al. (1997) (thin dotted line).

from density fluctuation spectrum in the early universe.

Figure 27 shows the contours of galaxy distribution in the cooling diagram for ellipticals (*top panel*), lenticulars (*middle panel*), and spirals (*bottom panel*). The velocity on the horizontal axis indicates the velocity dispersion of bulge component for elliptical and lenticular galaxies, and the disk rotation velocity for spiral galaxies. The baryon density on the vertical axis is estimated by dividing the baryonic mass in individual galaxies by their volume. We simply assume a sphere of effec-

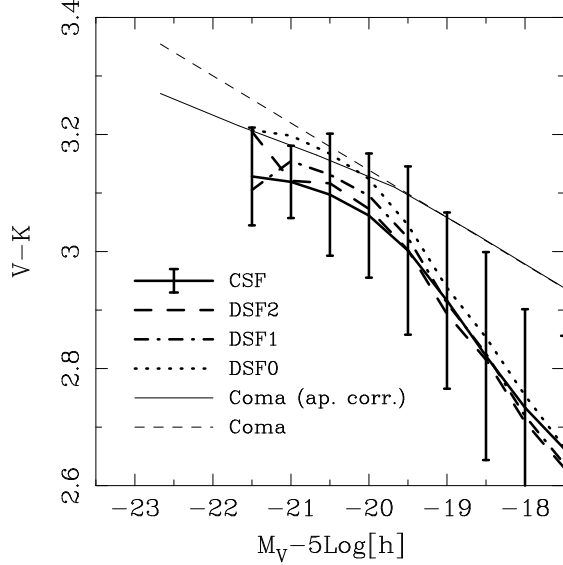


FIG. 24.— $V-K$ color-magnitude relation of elliptical galaxies in clusters. Such galaxies are sampled from the clusters having $V_c = 10^3 \text{ km s}^{-1}$, and the theoretical CMRs are shown for the models of CSF (thick solid line), DSF2 (thick dashed line), DSF1 (thick dot-dashed line), and DSF0 (thick dotted line), where the effects of dynamical response to starburst-induced gas removal are taken into account. The observed CMR for the Coma cluster is shown as a mean relation by Bower, Lucey & Ellis (1992) (thin dashed line), and the aperture-corrected CMR for the same cluster by Kodama et al. (1998) (thin solid line).

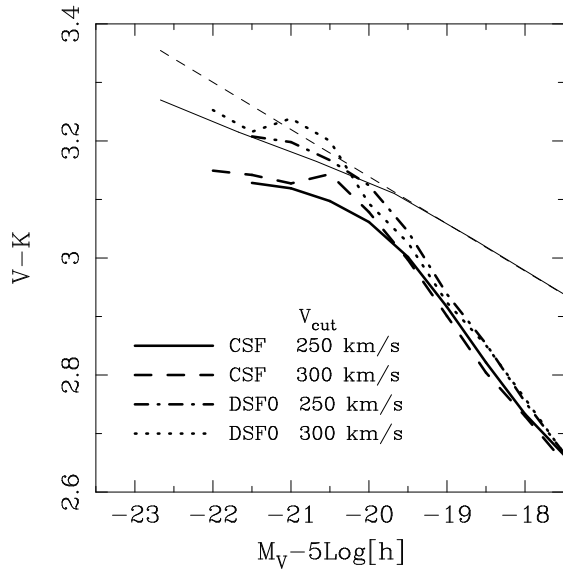


FIG. 25.— $V-K$ color-magnitude relation of elliptical galaxies in clusters. Same as Figure 24, but for the effect of changing V_{cut} . The thick solid and dashed lines show the theoretical CMRs in the CSF model with $V_{\text{cut}} = 250$ (our standard choice) and 300 km s^{-1} , respectively. The dot-dashed and dotted lines similarly show these two cases for the DSF0 model, respectively.

tive radius for elliptical and lenticular galaxies, and a cylinder of scale height being one tenth of the effective radius for spiral galaxies. The contours are plotted excluding low surface brightness galaxies with $\mu_{e,B} \geq 26.5$.

The dashed and dot-dashed lines represent the cooling curves that the cooling timescale is equal to the gravitational free-fall timescale $\tau_{\text{cool}} = \tau_{\text{grav}}$ for the cases of primordial and

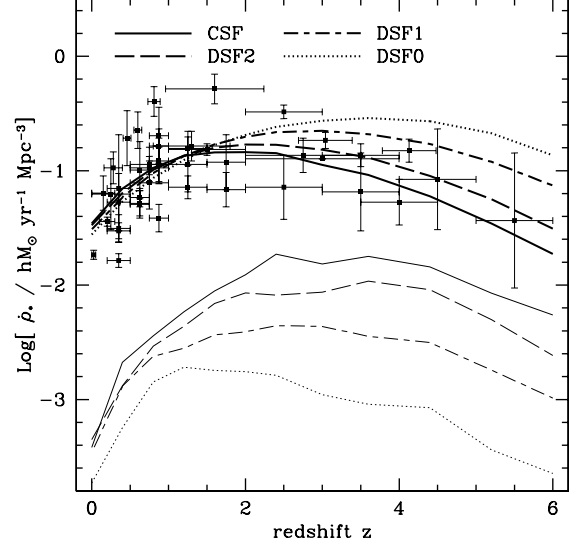


FIG. 26.— Cosmic Star Formation Histories. The solid, dashed, dot-dashed and dotted lines denote CSF, DSF2, DSF1 and DSF0, respectively. The thick lines indicate the total SFR and the thin lines the SFR only for starburst. Symbols with errorbars are observational data compiled by Ascasibar et al. (2002).

solar compositions, respectively. These timescales are

$$\tau_{\text{cool}} = \frac{3 \rho_{\text{gas}}}{2 \mu m_p n_e^2 \Lambda(T, Z_{\text{gas}})} \frac{kT}{}, \quad (21)$$

$$\tau_{\text{grav}} = (24\pi G \rho_{\text{tot}})^{-1/2}, \quad (22)$$

where n_e is the electron number density, ρ_{gas} is the gas density, ρ_{tot} is the total mass density including dark matter, and $\Lambda(T, Z_{\text{gas}})$ is the cooling function depending on both the gas temperature T and metallicity Z_{gas} . Wherever necessary below, we transform the gas temperature into velocity dispersion based on the virial theorem, and identify the gas density with baryon density. The thin solid curves represent the sequences of galaxies originated from the CDM density fluctuations with density contrast of 1σ and 3σ , respectively. It is evident from this figure that our SAM galaxies are distributed within a region of $\tau_{\text{cool}} < \tau_{\text{grav}}$ and their morphologies are distinctly segregated from each other, as observed in this diagram.

Figure 28 shows the distribution for all galaxies without imposing any selection bias against low surface brightness. Comparison of Figures 27 and 27 indicates that many dwarf galaxies have low surface brightness and are distributed towards a region of $\tau_{\text{cool}} > \tau_{\text{grav}}$ characterized by low baryon density and low circular velocity. This extended distribution is prominent only for elliptical galaxies for which the starburst-induced gas removal followed by dynamical response has the maximal effect. Such galaxies of low surface brightness would have been detected in recent ultra-deep surveys where the detection threshold is set below $\mu_{e,B} = 26.5$.

8. SUMMARY AND CONCLUSION

We have investigated the formation and evolution of galaxies in the context of the hierarchical clustering scenario by using the Mitaka model, or our SAM in which the effects of dynamical response on size and velocity dispersion of galaxies are explicitly taken into account, according to the formula by Nagashima & Yoshii (2003) for galaxies consisting of baryon and dark matter. This paper is therefore an extension of previ-

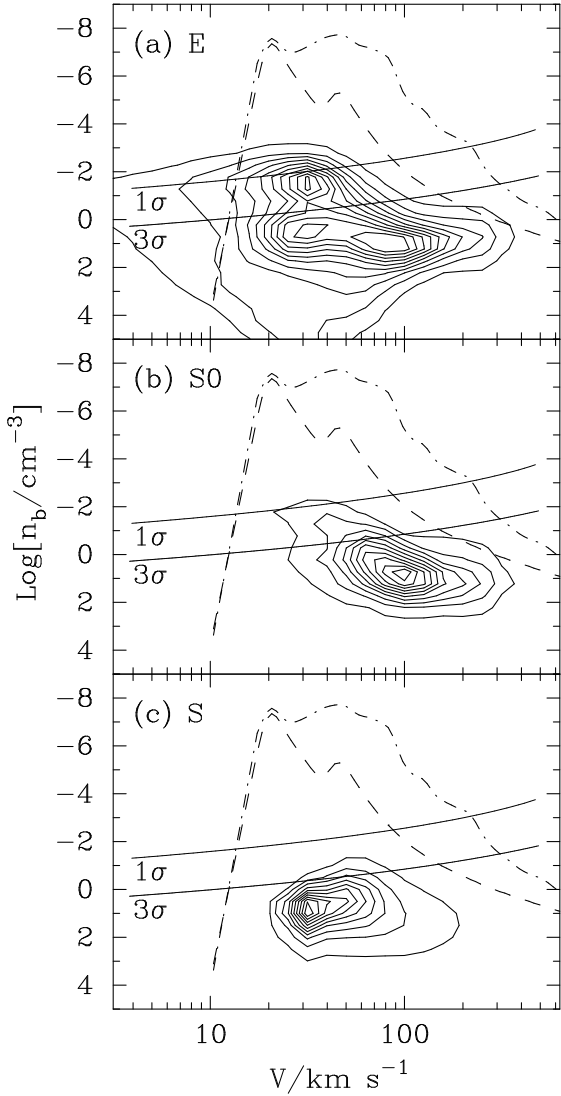


FIG. 27.—Cooling diagram for (a) elliptical galaxies, (b) lenticular galaxies, and (c) spiral galaxies. Contours indicate the theoretical distribution predicted by the CSF model with surface brightness cutoff at $\mu_{e,B} = 26.5$ and the effects of dynamical response taken into account in the analysis. The levels of contours are the same as in Figure 6. Top panel shows a broad distribution of elliptical galaxies consisting of dwarf ellipticals on the left and normal/giant ellipticals on the right, which are bifurcated reflecting a variety of star formation and merger histories. The dashed line represents $\tau_{\text{cool}} = \tau_{\text{grav}}$ for the gas of primordial chemical composition, and the dot-dashed line for the gas of solar chemical composition. The thin lines represent two sequences of collapse of overdense regions with 1σ and 3σ fluctuations against CDM spectrum.

ous analyses in the context of monolithic cloud collapse scenario (Dekel & Silk 1986; Yoshii & Arimoto 1987).

A Λ -dominated flat universe, which is recently recognized as a standard, is exclusively used here. The investigation mainly focuses on elliptical galaxies which are assumed to be formed by major merger and starburst-induced gas removal followed by dynamical response of the systems. While a mass fraction of removed cold gas, after heated, is determined by the circular velocity of galaxies similar to the traditional collapse models, the total amount of cold gas depends on the formation history of galaxies which is realized by the Monte Carlo method based on the power spectrum of density fluctuation predicted by the CDM model.

The Mitaka model, which we have constructed in this paper,

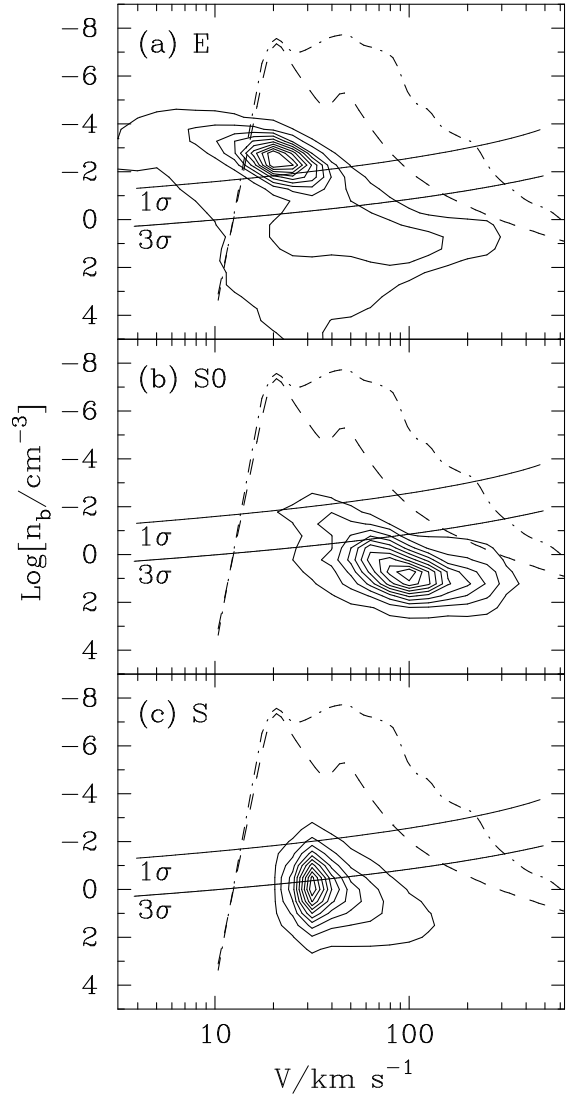


FIG. 28.—Cooling diagram. Same as Figure 27, but for all galaxies without imposing any selection bias against low surface brightness.

is found to reproduce a wide variety of observed characteristics of galaxies, particularly their scaling relations among various observables such as magnitude, surface brightness, size, velocity dispersion, mass-to-light ratio and metallicity. This strongly supports the CDM cosmology and merger hypothesis of elliptical galaxy formation even on scales of dwarf galaxies.

Most of model parameters related to star formation, SN feedback and galaxy merger are constrained by the local luminosity function and mass fraction of cold gas in spiral galaxies. As an extra parameter to be furthermore constrained, we have examined redshift dependence of SF timescale through comparison among the four SF models denoted by CSF, DSF0, DSF1, and DSF2. The CSF refers to a constant SF timescale against redshift and has been suggested to be consistent with observations of galaxy number counts (Nagashima et al. 2001, 2002), quasar luminosity function (Kauffmann & Haehnelt 2000; Enoki, Nagashima & Gouda 2003), and number and metallicity evolution of damped Ly- α systems (Somerville, Primack & Faber 2001; Okoshi et al. 2002). The DSF0 refers to a SF timescale simply proportional

to dynamical timescale. The DSF1 and DSF2 are intermediate between the CSF and DSF0 (see Figure 2). It is found that the DSF0 model fails to reproduce observed properties of local dwarf spheroidals and galaxy counts. Among the above four SF models, the CSF model has the longest SF timescale at high redshift and therefore the largest amount of cold gas at that epoch. Accordingly, the fraction of removed gas during starburst is the largest in the CSF model, giving many extended galaxies in agreement with observation. In this sense, the model of constant star formation (CFS) or at most mildly evolving star formation (DSF2) is favorable. Note that *dominant dark halo*, in which size and velocity dispersion do not change during gas removal as considered by Dekel & Silk (1986), apparently explains the observed scatter of size. However, arguments from physical ground indicate that the dynamical response should play a significant role in forming galaxies with low velocity dispersion of $\sigma_0(1D) \lesssim 10\text{km s}^{-1}$, as actually observed in the Local Group.

There are some areas of further improvements in the current Mitaka model. Because of strong dependence of SN feedback on circular velocity assuming $\alpha_{\text{hot}} = 4$, dwarf galaxies in our SF models are too faint to agree with expected magnitude from observed TFRs. Furthermore, because of the same reason, dwarf galaxies are too blue to agree with expected colors from observed CMRs for cluster elliptical galaxies. On the other hand, such large value of α_{hot} stops chemical and photometric evolution of elliptical galaxies at early epochs and is required to explain their observed low stellar metallicity as well as the galaxy number counts in the HDF and SDF. In order to settle these contradictions, some new ingredients need to be introduced in the SAM analysis. At least, for example,

we must know how efficient the gas cooling is in massive dark halos and whether SN feedback at starburst works in the same way as that in disks.

We adopted a fitting mass function of dark halos by Yahagi, Nagashima & Yoshii (2003) for given redshift instead of the often used PS mass function. This YNY mass function is slightly different from those by Sheth & Tormen (1999) and Jenkins et al. (2001), but is confirmed to provide a better fit to recent N -body results given by Yahagi & Yoshii (2001) and Yahagi (2002), which is discussed in more detail in a separate paper (Yahagi, Nagashima & Yoshii 2003). Since the number density of dark halos affects SN feedback-related parameters to be chosen, it is very important to establish the mass function of dark halos, particularly on small mass scales, by high resolution N -body simulation. Although such SAM analyses have just begun (e.g., Benson et al. 2001; Helly et al. 2003a,b), further investigation will obviously be required. We are upgrading the Mitaka model accommodated with full high resolution N -body simulations, and the results will be given elsewhere in the near future.

We thank Takashi Okamoto and Naoteru Gouda for useful suggestions. The authors are grateful to the anonymous referee for helpful comments to improve this paper. This work has been supported in part by the Grant-in-Aid for the Center-of-Excellence research (07CE2002) of the Ministry of Education, Science, Sports and Culture of Japan. MN acknowledges support from a PPARC rolling grant for extragalactic astronomy and cosmology.

APPENDIX

DYNAMICAL RESPONSE TO GAS REMOVAL

We show the dynamical response of size and velocity dispersion to supernova-induced gas removal in the two-component galaxies consisting of baryon and dark matter. The details are given in Nagashima & Yoshii (2003).

All elliptical galaxies in this paper have a density profile similar to the Jaffe model (Jaffe 1983),

$$\rho(r) = \frac{4\rho_b r_b^4}{r^2(r+r_b)^2}, \quad (\text{A1})$$

where ρ_b and r_b are the characteristic density and radius, respectively. This profile well approximate the de Vaucouleurs $r^{1/4}$ profile for stars. The effective (half-light) radius r_e defined in the projected surface is related to the half-mass radius r_b in three dimensional space as $r_e = 0.744r_b$ (Nagashima & Yoshii 2003). For the distribution of dark matter, the singular isothermal distribution ($\rho_d \propto r^{-2}$) is considered. We found that the Navarro-Frenk-White profile (Navarro, Frenk & White 1997) provides almost the same results as those given by singular isothermal sphere. Note that according to recent high resolution N -body simulations, which have reveals that many substructures survive even in virialized halos, we assume that subhalos exist as underlying gravitational potential for satellite galaxies. As mentioned in §2.2, these subhalos are tidally truncated.

Because the derivation is long and complicated, we describe it only briefly. Just after the merger, the system is virialized immediately. Then the starburst occurs and a part of gas is gradually removed. The size and velocity dispersion change following the gas removal adiabatically. During the gas removal, the dark matter distribution is assumed to be not affected.

In the followings we derive useful simplified formulae for the dynamical response. As shown in Appendix B of Nagashima & Yoshii (2003), the relationship between density and size for the adiabatic gas removal is given by

$$Y = \frac{h(y_i, z_i)p(z_f) + q(z_f)}{y_i}, \quad (\text{A2})$$

where $Y \equiv y_f/y_i$, $y_i = \rho_i/\rho_d$, $z_{i,f} = r_{i,f}/r_d$, and the function h, p and q are

$$h(y, z) = yz^4 + \frac{1}{2}[-z + (1+z)\ln(1+z)], \quad (\text{A3})$$

$$p(z) = \frac{1}{z^4}, \quad (\text{A4})$$

$$q(z) = -\frac{1}{2z^4}[-z + (1+z)\ln(1+z)]. \quad (\text{A5})$$

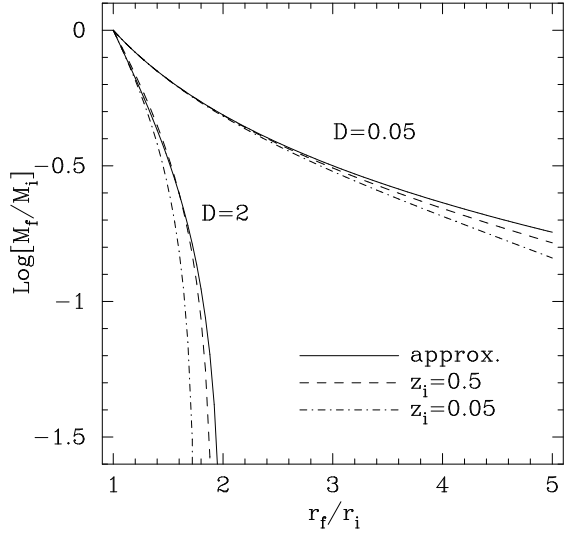


FIG. 29.— Dynamical response of galaxy size to removed mass from the system. The approximate results given by equation (A9) are shown for $D = 0.05$ and 0.2 (solid lines). For each value of D , the exact results given by equation (A6) are shown for $z_i = 0.5$ (dashed lines) and 0.05 (dot-dashed lines).

In order to obtain the size after gas removal, we need to know the inverted function of the above and it will be very complicated. Therefore, we approximate the above function. The equation can be reduced to the following expression,

$$Y = \frac{1}{R^4} + \frac{U_{\text{iso}}(R, z_i)}{2y_i z_i^4 R^4}, \quad (\text{A6})$$

where $R = z_f/z_i$. Expanding $U_{\text{iso}}(R, z_i)$ around $R = 1$ and $z_i = 0$ and picking out the lowest order term, we obtain

$$Y = \frac{1}{R^4} - \frac{D}{2} \frac{R-1}{R^4}, \quad (\text{A7})$$

where $D = 1/y_i z_i^2$. Defining the ratio of final to initial masses, $\mathcal{M} = M_f/M_i = YR^3$, the above equation is transformed to

$$\mathcal{M} = \frac{1}{R} - \frac{D}{2} \frac{R-1}{R}. \quad (\text{A8})$$

Then, inverting this, we obtain

$$R = \frac{1+D/2}{\mathcal{M}+D/2}. \quad (\text{A9})$$

By using the virial theorem, the velocity dispersion is

$$\frac{\sigma_f}{\sigma_i} = \sqrt{\frac{YR^2 + Df(z_f)/2}{1 + Df(z_i)/2}}, \quad (\text{A10})$$

where

$$f(z) = \frac{\ln(1+z)}{z} + \ln\left(1 + \frac{1}{z}\right). \quad (\text{A11})$$

Figure 29 shows the relation between \mathcal{M} and R based on this approximate formula with $D = 0.05$ and 2 (solid lines). For each value of D , the exact solution is also shown for two cases of $z_i = 0.05$ (dot-dashed line) and 0.5 (dashed line). Clearly our approximate relation follows the exact solution quite well.

REFERENCES

- Ascasibar Y., Yepes G., Gottlöber S., Müller V., 2002, *A&A*, 387, 396
 Arimoto, N., & Yoshii, Y. 1986, *A&A*, 164, 260
 Arimoto, N., & Yoshii, Y. 1987, *A&A*, 173, 23
 Arimoto, N., Yoshii, Y., & Takahara, F. 1991, *A&A*, 253, 21
 Bardeen, J. M., Bond, J. R., Kaiser, N., & Szalay, A. S. 1986, *ApJ*, 304, 15
 Baum, W. A. 1959, *PASP*, 71, 106
 Baugh, C. M., Cole, S., & Frenk, C. S. 1996, *MNRAS*, 283, 1361
 Baugh, C. M., Cole, S., Frenk, C. S., & Lacey, C. G. 1998, *ApJ*, 498, 504
 Bender, R., Burstein, D., & Faber, S. M. 1992, *ApJ*, 399, 462
 Bender, R., Burstein, D., & Faber, S. M. 1993, *ApJ*, 411, 153
 Bender, R., Paquet, A., & Nieto, J.-L. 1991, *A&A*, 246, 349
 Benson, A. J., Pearce, F. R., Frenk, C. S., Baugh, C. M., & Jenkins, A. 2001, *MNRAS*, 320, 261
 Benson, A. J., Lacey, C. G., Baugh, C. M., Cole, S., & Frenk, C. S. 2002a, *MNRAS*, 333, 156
 Benson, A. J., Frenk, C. S., Lacey, C. G., Baugh, C. M., & Cole, S. 2002b, *MNRAS*, 333, 177

- Benson, A. J., Frenk, C. S., Baugh, C. M., Cole, S., & Lacey, C. G. 2003a, *MNRAS*, 343, 679
- Benson, A. J., Bower, R. G., Frenk, C. S., Lacey, C. G., Baugh, C. M., & Cole, S. 2003b, preprint (astro-ph/0302450)
- Binney, J., & Tremaine, S. 1987, *Galactic Dynamics*, Princeton Univ. Press, Princeton, NJ
- Blumenthal, G. R., Faber, S. M., Primack, J. R., & Rees, M. J. 1984, *Nature*, 311, 517
- Bond, J. R., Cole, S., Efstathiou, G., & Kaiser, N. 1991, *ApJ*, 379, 440
- Bower, R. 1991, *MNRAS*, 248, 332
- Bower, R., Lucey, J.R., & Ellis, R.S. 1992, *MNRAS*, 254, 601
- Bullock, J. S., Kravtsov, A. V., & Weinberg, D. H. 2000, *ApJ*, 517, 521
- Catelan, P., & Theuns, T. 1996a, *MNRAS*, 282, 436
- Catelan, P., & Theuns, T. 1996b, *MNRAS*, 282, 455
- Chiba, M., & Nath, B.B. 1994, *ApJ*, 436, 618
- Ciotti, L., Pellegrini, S. 1992, *MNRAS*, 255, 561
- Cole, S., Aragon-Salamanca, A., Frenk, C. S., Navarro, J. F., & Zepf, S. E. 1994, *MNRAS*, 271, 781
- Cole, S., Lacey, C. G., Baugh, C. M., & Frenk, C. S. 2000, *MNRAS*, 319, 168
- Cole, S. et al. 2001, *MNRAS*, 326, 255
- Dekel A., Silk J., 1986, *ApJ*, 303, 39
- Disney, M., Davies, J., & Phillips, S. 1989, *MNRAS*, 239, 939
- Djorgovski, S., & Davis, M. 1987, *ApJ*, 313, 59
- Dressler, A., Lynden-Bell, D., Burstein, D., Davies, R. L., Faber, S. M., Terlevich, R. J., & Wegner, G. 1987, *ApJ*, 313, 42
- EGGEN, O.J., LYNDEN-BELL, D., & SANDAGE, A.R. 1962, *ApJ*, 136, 748
- Enoki, M., Nagashima, M., & Gouda, N. 2003, *PASJ*, 55, 133
- Faber S.M., 1982, in Brück H. A., Coyne G. V., Longair M. S., eds, *Astrophysical Cosmology*, Pontificia Academia Scientiarum, p. 191
- Faber, S. M., & Jackson, R. E. 1976, *ApJ*, 204, 668
- Fall, S. M. 1979, *Nature*, 281, 200
- Fall, S. M., & Efstathiou, G. 1980, *MNRAS*, 193, 189
- Fall, S. M. 1983, in 'Internal kinematics and dynamics of galaxies', proceedings of the IAU symposium 100, Besancon, France, Dordrecht, D. Reidel, p.391
- Fernández-Soto, A., Lanzetta, K. M., & Yahil, A. 1999, *ApJ*, 513, 34
- Folk, S. et al. 1999, *MNRAS*, 308, 459
- Furusawa, H., Shimasaku, K., Doi, M., & Okamura, S. 2000, *ApJ*, 534, 624
- Gardner, J. P., Sharples, R. M., Carrasco, B. E., & Frenk, C. S. 1996, *MNRAS*, 282, L1
- Ghigna, S., Moore, B. Governato, F., Lake, G., Quinn, T., & Stadel, J. 1998, *ApJ*, 300, 146
- Giovanelli, R., Haynes, M.P., da Costa, L.N., Freudling, W., Salzer, J.J., & Wegner, G. 1997, *ApJ*, 477, L1
- Glazebrook, K., Peacock, J.A., Miller, L., & Collins, C.A. 1994, *MNRAS*, 266, 65
- Gunn, J.E., & Gott, J.R. 1972, *ApJ*, 176, 1
- Hall, P., & Mackay, C. B. 1984, *MNRAS*, 210, 979
- Held, E. V., de Zeeuw, T., Mould, J., & Picard, A. 1992, *AJ*, 103, 851
- Helly, J. C., Cole, S., Frenk, C. S., Baugh, C. M., Benson, A. J., & Lacey, C. 2003, *MNRAS*, 338, 903
- Helly, J. C., Cole, S., Frenk, C. S., Baugh, C. M., Benson, A. J., Lacey, C., & Pearce, F. R. 2003, *MNRAS*, 338, 913
- Hills, J. G. 1980, *ApJ*, 225, 986
- Huchtmeier, W. K., & Richter, O. -G. 1988, *A&A*, 203, 237
- Ikeuchi, S. 1977, *PTP*, 58, 1742
- Impey, C.D., Sprayberry, D., Irwin, M. J., & Bothun, G. D. 1996, *ApJS*, 105, 209
- Jaffe, W. 1983, *MNRAS*, 202, 995
- Jenkins, A., Frenk, C. S., White, S. D. M., Colberg, J. M., Cole, S., Evrard, A. E., Couchman, H. M. P., & Yoshida, N. 2001, *MNRAS*, 321, 372
- Jones, L.R., Fong, R., Shanks, T., Ellis, R. S., & Peterson, B. A. 1991, *MNRAS*, 249, 481
- Kauffmann, G., & Charlot, S. 1998, *MNRAS*, 294, 705
- Kauffmann, G., & Haehnelt, M. 2000, *MNRAS*, 311, 576
- Kauffmann, G., White, S. D. M., & Guiderdoni, B. 1993, *MNRAS*, 264, 201
- Kawata, D., & Gibson, B.K. 2003, *MNRAS*, 340, 908
- Kochanek, C.S. et al. 2001, *ApJ*, 560, 566
- Kodaira, K., Okamura, S., & Watanabe, M. 1983, *ApJ*, 274, L49
- Kodama, T., & Arimoto, N. 1997, *A&A*, 320, 41
- Kodama, T., Arimoto, N., Barger, A.J., & Aragón-Salamanca A. 1998, *A&A*, 334, 99
- Koo, D.C. 1986, *ApJ*, 311, 651
- Kormendy, J. 1977, *ApJ*, 218, 333
- Lacey, C.G., & Cole, S. 1993, *MNRAS*, 262, 627
- Larson, R. B. 1969, *MNRAS*, 169, 229
- Loveday, J., Peterson, B. A., Efstathiou, G., & Maddox, S. J. 1992, *ApJ*, 90, 338
- Madau, P., Ferguson, H., Dickinson, M., Giavalisco, M., Steidel, C., & Fruchter, A. 1996, *MNRAS*, 283, 1388
- Maddox, S. J., Sutherland, W. J., Efstathiou, G., Loveday, J., & Peterson, B. A. 1990, *MNRAS*, 247, 1p
- Maihara, T. et al. 2001, *PASJ*, 53, 25
- Makino, J., & Hut, P. 1997, *ApJ*, 481, 83
- Mateo, M. L. 1998, *ARA&A*, 36, 435
- Mathewson, D.S., Ford, V.L., & Buchhorn, M. 1992, *ApJS*, 81, 413
- Mathieu, R. D. 1983, *ApJ*, 267, L97
- McLeod, B.A., Bernstein, G.M., Rieke, M.J., Tollestrup, E.V., & Fazio, G.G. 1995, *ApJS*, 96, 117
- Metcalfe, N., Shanks, T., Fong, R., & Jones, L. R. 1991, *MNRAS*, 249, 498
- Minezaki, T., Kobayashi, Y., Yoshii, Y., & Peterson, B.A. 1998, *ApJ*, 494, 111
- Mo, H.J., Mao, S., & White, S.D.M. 1998, *MNRAS*, 295, 319
- Monaco, P. 1998, *Fundam. Cosmic Phys.*, 19, 157
- Nagashima, M. 2001, *ApJ*, 562, 7
- Nagashima, M., & Gouda, N. 1998, *MNRAS*, 301, 849
- Nagashima, M., Gouda, N., & Sugiura, N. 1999, *MNRAS*, 305, 449
- Nagashima, M., & Gouda, N. 2001, *MNRAS*, 325, L13
- Nagashima, M., Totani, T., Gouda, N., & Yoshii, Y. 2001, *ApJ*, 557, 505
- Nagashima, M., Yoshii, Y., Totani, T., & Gouda, N. 2002, *ApJ*, 578, 675
- Nagashima, M., & Yoshii, Y. 2003, *MNRAS*, 340, 509
- Navarro, J. F., Frenk, C. S., & White, S. D. M. 1997, *ApJ*, 490, 493
- Netterfield, C. B. et al. 2002, *ApJ*, 571, 604
- Okamoto, T., & Habe, A. 1999, *ApJ*, 516, 591
- Okamoto, T., & Habe, A. 2000, *PASJ*, 52, 457
- Okamoto, T., & Nagashima, M. 2003, *ApJ*, 587, 500
- Okoshi, K., Nagashima, M., Gouda, N., & Yoshioka, S. 2004, *ApJ*, in press
- Ostriker, J.P. & Gnedin, N.Y. 1996, *ApJ*, 472, L63
- Pierce, M., & Tully, R.B. 1992, *ApJ*, 387, 47
- Press, W., & Schechter, P. 1974, *ApJ*, 187, 425
- Ratcliffe, A., Shanks, T., Parker, Q., & Fong, R. 1998, *MNRAS*, 293, 197
- Rees, M.J., & Ostriker, J.P. 1977, *MNRAS*, 179, 541
- Saito, M. 1979, *PASJ*, 31, 193
- Seaton, M. J. 1979, *MNRAS*, 187, 73P
- Sheth, R., & Tormen, G. 1999, *MNRAS*, 308, 119
- Silk, J. 1977, *ApJ*, 211, 638
- Simard, L., Koo, D. C., Faber, S. M., Sarajedini, V. L., Vogt, N. P., Phillips, A. C., Gebhardt, K., Illingworth, G. D., & Wu, K. L. 1999, *ApJ*, 519, 563
- Simien, F., & de Vaucouleurs, G. 1986, *ApJ*, 302, 564
- Somerville, R. S. 2002, *ApJ*, 572, 23
- Somerville, R.S., & Kolatt, T. 1999, *MNRAS*, 305, 1
- Somerville, R.S., & Primack, J. R. 1999, *MNRAS*, 310, 1087
- Somerville, R.S., Primack, J. R., & Faber, S. M. 2001, *MNRAS*, 320, 504
- Spergel, D.N. et al. 2003, preprint (astro-ph/0302209)
- Sugiyama, N. 1995, *ApJS*, 100, 281
- Sutherland, R., & Dopita, M. A. 1993, *ApJS*, 88, 253
- Suzuki, T.K., Yoshii, Y., & Beers, T.C. 2000, *ApJ*, 540, 99
- Szkoly, G.P., Subbarao, M.U., Connolly, A.J., & Mobasher, B. 1998, *ApJ*, 492, 452
- Tomita, K. 1969, *Prog. Theor. Phys.*, 42, 9
- Totani, T., & Yoshii, Y. 2000, *ApJ*, 540, 81
- Totani, T., Yoshii, Y., Maihara, T., Iwamuro, F., & Motohara, K. 2001, *ApJ*, 559, 592
- Tully, R. B., Somerville, R. S., Trentham, N., & Verheijen, M. A. W. 2002, *ApJ*, 569, 573
- Tyson, J.A. 1988, *AJ*, 96, 1
- Vader, J. P. 1986, *ApJ*, 305, 669
- White, S.D.M. 1984, *ApJ*, 286, 38
- Williams, R. T. et al. 1996, *AJ*, 112, 1335
- Yahagi, H., & Yoshii, Y. 2001, *ApJ*, 558, 463
- Yahagi, H. 2002, D. Thesis, University of Tokyo
- Yahagi, H., Nagashima, M., & Yoshii, Y. 2003, submitted
- Yano, T., Nagashima, M., & Gouda, N. 1996, *ApJ*, 466, 1
- Yoshii, Y. 1993, *ApJ*, 403, 552
- Yoshii, Y., & Arimoto, N. 1987, *A&A*, 188, 13
- Yoshii, Y., & Peterson, B. A. 1994, *ApJ*, 436, 551
- Yoshii, Y., & Saio, H. 1979, *PASJ*, 31, 339
- Yoshii, Y., & Saio, H. 1987, *MNRAS*, 227, 677
- Yoshii, Y., & Takahara, F. 1988, *ApJ*, 326, 1
- Watanabe, M., Kodaira, K., & Okamura, S. 1985, *ApJ*, 292, 72
- Zucca, E. et al. 1997, *A&A*, 326, 477